

# Gasdermin-E-mediated pyroptosis drives immune checkpoint inhibitor-associated myocarditis via cGAS-STING activation

Received: 24 October 2023

Accepted: 23 July 2024

Published online: 05 August 2024

 Check for updates

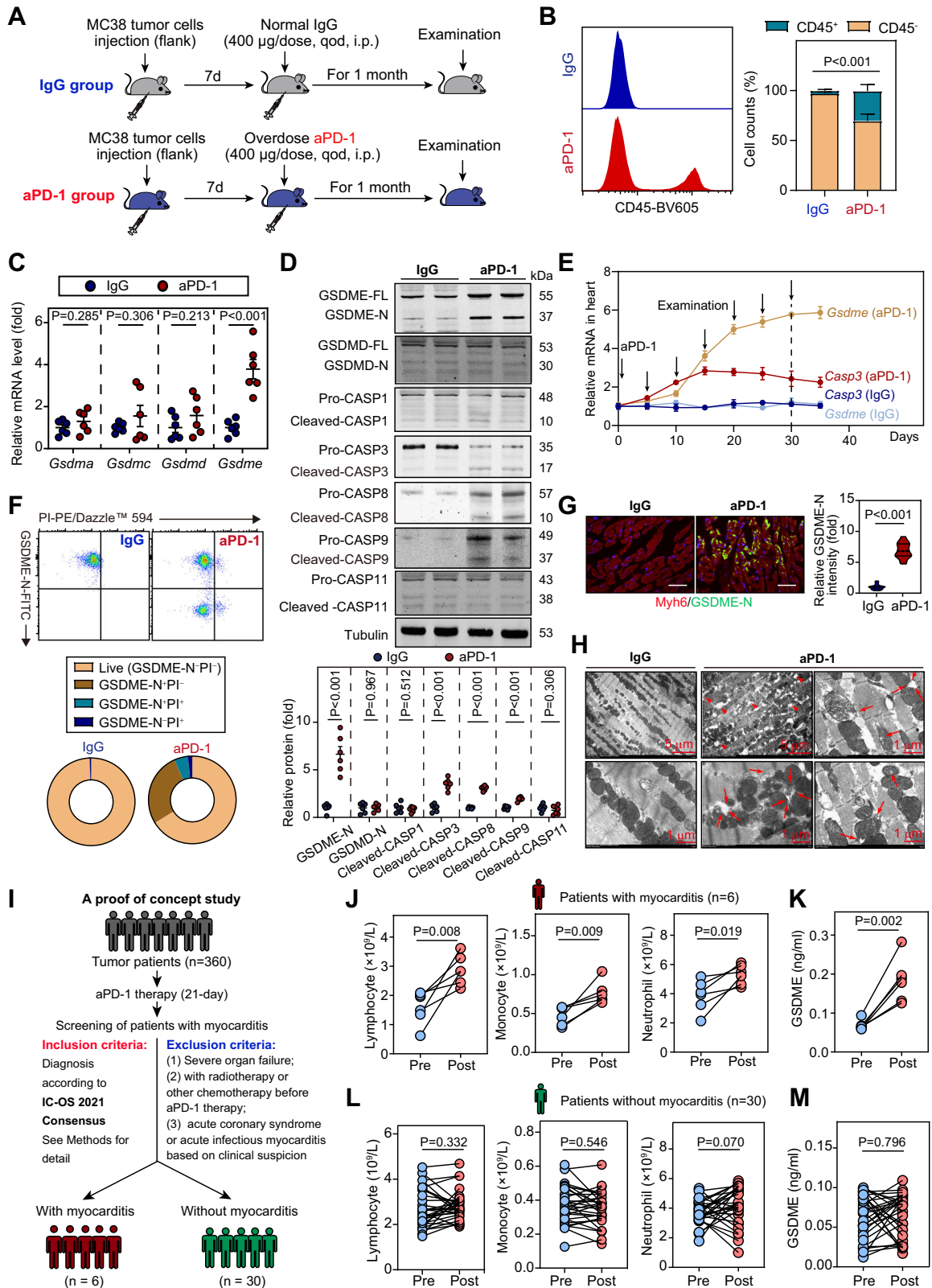
Si-Jia Sun<sup>1,2,9</sup>, Xiao-Dong Jiao<sup>3,9</sup>, Zhi-Gang Chen<sup>4,9</sup>, Qi Cao<sup>2,9</sup>, Jia-Hui Zhu<sup>1</sup>, Qi-Rui Shen<sup>5</sup>, Yi Liu<sup>1</sup>, Zhen Zhang<sup>1</sup>, Fang-Fang Xu<sup>1</sup>, Yu Shi<sup>1</sup>, Jie Tong<sup>1</sup>, Shen-Xi Ouyang<sup>1</sup>, Jiang-Tao Fu<sup>2</sup>, Yi Zhao<sup>1</sup>, Jun Ren<sup>6</sup>, Dong-Jie Li<sup>1</sup>✉, Fu-Ming Shen<sup>1</sup>✉ & Pei Wang<sup>2,7,8</sup>✉

Immune checkpoint inhibitor (ICI)-induced myocarditis involves intensive immune/inflammation activation; however, its molecular basis is unclear. Here, we show that gasdermin-E (GSDME), a gasdermin family member, drives ICI-induced myocarditis. Pyroptosis mediated by GSDME, but not the canonical GSDMD, is activated in myocardial tissue of mice and cancer patients with ICI-induced myocarditis. Deficiency of GSDME in male mice alleviates ICI-induced cardiac infiltration of T cells, macrophages, and monocytes, as well as mitochondrial damage and inflammation. Restoration of GSDME expression specifically in cardiomyocytes, rather than myeloid cells, in GSDME-deficient mice reproduces ICI-induced myocarditis. Mechanistically, quantitative proteomics reveal that GSDME-dependent pyroptosis promotes cell death and mitochondrial DNA release, which in turn activates cGAS-STING signaling, triggering a robust interferon response and myocardial immune/inflammation activation. Pharmacological blockade of GSDME attenuates ICI-induced myocarditis and improves long-term survival in mice. Our findings may advance the understanding of ICI-induced myocarditis and suggest that targeting the GSDME-cGAS-STING-interferon axis may help prevent and manage ICI-associated myocarditis.

Immunotherapy has fundamentally changed the treatment landscape for cancer. Immune-checkpoint inhibitors (ICI), which trigger immune response by targeting programmed cell death 1 (PD-1), programmed cell death 1 ligand 1 (PD-L1) and cytotoxic T lymphocyte antigen 4

(CTLA-4), are increasingly used. However, use of ICI has drastically increased the incidence of immune-related adverse events (irAEs)<sup>1</sup>. ICI-associated fatal myocarditis is the first described cardiac irAEs, with a low prevalence of ~1% and a high mortality of ~50%<sup>2,3</sup>. Meanwhile, ICI

<sup>1</sup>Department of Pharmacy, Shanghai Tenth People's Hospital, School of Medicine, Tongji University, Shanghai, China. <sup>2</sup>The Center for Basic Research and Innovation of Medicine and Pharmacy (MOE), School of Pharmacy, Naval Medical University/Second Military Medical University, Shanghai, China. <sup>3</sup>Department of Oncology, Changzheng Hospital, Naval Medical University/Second Military Medical University, Shanghai, China. <sup>4</sup>Department of Anesthesiology, Shanghai Pulmonary Hospital, School of Medicine, Tongji University, Shanghai, China. <sup>5</sup>Department of Pharmacy, Shanghai Skin Disease Hospital, Tongji University School of Medicine, Shanghai, China. <sup>6</sup>Department of Cardiology and Shanghai Institute of Cardiovascular Disease, Zhongshan Hospital, Fudan University, Shanghai, China. <sup>7</sup>Shanghai Key Laboratory for Pharmaceutical Metabolite Research, Naval Medical University/Second Military Medical University, Shanghai, China. <sup>8</sup>The National Demonstration Center for Experimental Pharmaceutical Education, Naval Medical University/Second Military Medical University, Shanghai, China. <sup>9</sup>These authors contributed equally: Si-Jia Sun, Xiao-Dong Jiao, Zhi-Gang Chen, Qi Cao. ✉e-mail: [djli@tongji.edu.cn](mailto:djli@tongji.edu.cn); [fumingshen@tongji.edu.cn](mailto:fumingshen@tongji.edu.cn); [pwang@smmu.edu.cn](mailto:pwang@smmu.edu.cn)



induced other types of cardiac irAEs, including transient ischemic attack, acute coronary syndrome, heart failure, arrhythmias, large artery inflammation, and possibly atherosclerosis, with a much higher prevalence (up to ~10%) than previously appreciated<sup>4-6</sup>. The abnormally activated T-cells and macrophages/monocytes may play key roles in ICI-induced myocarditis<sup>7-11</sup>. However, the molecular basis of the ICI-associated myocarditis is still unclear. Especially, the immune-

modulatory pathological mechanisms underlying the immune/inflammation activation subsequent to the overwhelming accumulation of T-cells and monocytes/macrophages (MOs/MPs) in heart, remain to be elucidated.

Pyroptosis, an inflammatory form of regulated cell death (RCD)<sup>12</sup>, is characterized by inflammasomes activation and gasdermins (GSDMs)-mediated membrane pores formation<sup>13</sup>. Generally, caspase-1

**Fig. 1 | GSDME-mediated pyroptosis is activated in mouse and cancer patients received aPD-1 therapy.** **A** Experimental protocol for the mouse model of myocarditis-induced by a prolonged overdose aPD-1 therapy. **B** The proportion of CD45<sup>+</sup> leukocytes (including myeloid and lymphoid cells) in hearts of IgG or aPD-1-treated mice were determined using flow cytometry. *n* = 6 biologically independent experiments. **C** Gene expression of *Gsdma*, *Gsdmc*, *Gsdmd* and *Gsdme* in heart of mice received overdose aPD-1 therapy or normal IgG. *n* = 6 biologically independent experiments. **D** Immunoblotting showing the cleavages of GSDME, GSDMD, caspase-1, caspase-3, caspase-8, caspase-9 and caspase-11 in heart of mice with aPD-1-induced myocarditis. *n* = 6-7 biologically independent experiments. *n* = 6 biologically independent experiments. **E** The mRNA levels of *caspase-3* and *Gsdme* in heart tissue of IgG or aPD-1-treated mice at different time-points. *n* = 6 biologically independent experiments. **F** Flow cytometry showing the cells undergoing pyroptosis in heart of mice received aPD-1 therapy or normal IgG control. *n* = 6 biologically independent experiments. Single cells isolated from hearts were incubating with antibody against N-terminal of GSDME (GSDME-N) for 2 h and FITC-conjugated secondary antibody for 30 min. The samples were incubated with propidium iodide (PI) for detecting dead cell. **G** Fluorescent

immunohistochemistry showing the existence of GSDME-N in heart of mice. received aPD-1 therapy or normal IgG control. Scale bar, 50  $\mu$ m. *n* = 14 biologically independent experiments. **H** Transmission electron microscopy (TEM) showing the mitochondrial pores or penetrations (arrows) in heart tissue of mice received aPD-1 treatment. *n* = 6 biologically independent experiments. Scale bar, 5  $\mu$ m and 1  $\mu$ m. **I** Study design of a proof-of-concept investigation for detecting the role of GSDME in aPD-1-induced myocarditis in clinical patients. A total of six patients with myocarditis post aPD-1 treatment were identified according International Society of Cardio-Oncology (IC-OS) 2021 Consensus. Other 30 patients without myocarditis post aPD-1 treatment were used as control. **J**, **K** Comparisons of circulating numbers of immune cells (lymphocytes, monocyte and neutrophils, **J**) and serum level of GSDME (**K**) in six tumor patients with myocarditis pre- and post-aPd-1 therapy. **L**, **M** Comparisons of circulating numbers of immune cells (lymphocytes, monocyte and neutrophils, **L**) and serum level of GSDME (**M**) in 30 tumor patients without myocarditis pre- and post-aPd-1 therapy. The data were presented as means  $\pm$  SEM and analyzed by two-sided paired Student's t-tests (**J–M**) and two-sided unpaired Student's t-tests (other panels).

or caspase-11 cleaves gasdermin-D (GSDMD) to generate an active pore-forming N-terminal fragment (GSDMD-N), which is the major and final executor of canonical pyroptosis<sup>14,15</sup>. Recently, it has been known that caspase-3, the classical executor of apoptosis, cleaves another gasdermin family protein gasdermin-E (GSDME), converting the non-inflammatory apoptosis to pyroptosis<sup>16</sup>. GSDME acts as a tumour suppressor by activating immune cells including macrophages, natural-killer and CD8<sup>+</sup>-T lymphocytes recruitment into tumour<sup>17,18</sup>. Thus, GSDME is proposed as a potential ally in cancer therapy due to its potent anti-tumour activity. However, unlike GSDMD, GSDME is silenced in most cancer cells but expressed abundantly in normal tissues<sup>16</sup>, implying GSDME may modulates pyroptosis-related autoinflammation responses in normal tissue.

Given that the inflammatory pyroptotic death critically contributes to autoinflammation<sup>19,20</sup>, we explored, in this study, the role of pyroptosis in ICI-induced myocarditis. Our findings reveal that the pyroptosis-mediated by GSDME in cardiomyocytes, rather than immune cells, facilitates ICI-associated myocarditis via mediating mitochondrial damage and releasing mitochondrial DNA (mtDNA), which further activates cyclic GMP-AMP synthase (cGAS)-stimulator of interferon genes (STING) signaling pathway. These results may advance our understanding of the immunity and inflammation modulatory responses within myocardium subsequent to the infiltrated T-cells and macrophages/monocytes, and suggest targeted inhibition of GSDME-cGAS-STING axis may be a potential strategy for prevention/management of ICI-associated myocarditis.

## Results

### Activated GSDME-mediated pyroptosis by aPD-1-therapy is associated with myocarditis in mice and clinical patients

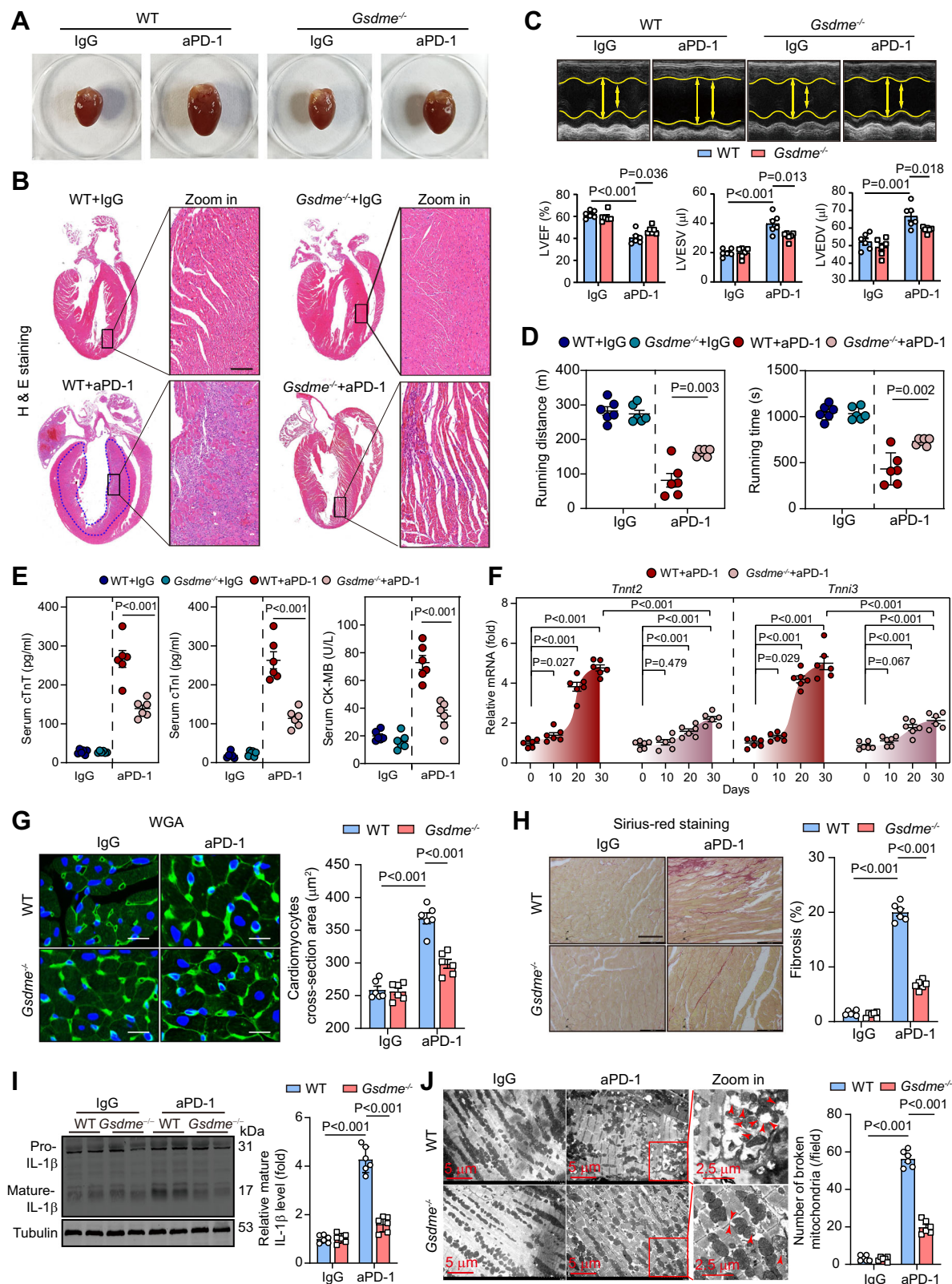
We developed a mouse model with aPD-1-induced myocarditis by injecting the mice bearing MC38 cells-derived tumor in flank with a prolonged aPD-1 treatment by administering overdose anti-mouse PD-1 for one month (Fig. 1A). This approach aimed to mimic the clinical scenario where cancer patients are treated solely with anti-PD-1 antibody, as approximately 70% of total cardiac irAEs are attributed to the administration of anti-PD-1 antibody alone<sup>21</sup>. Treatment of aPD-1 successfully inhibited tumor growth (Supplementary Fig. 1A) and inhibited tumor-induced death (Supplementary Fig. 1B). Flow cytometry showed that the number of CD45<sup>+</sup> leukocyte was increased in heart of mice received aPD-1 treatment (Fig. 1B). Accordingly, the aPD-1-treated mice exhibited myocardial infiltrations of T-cells (CD4<sup>+</sup> and CD8<sup>+</sup>) and macrophages/monocytes (CD68<sup>+</sup>, Supplementary Fig. 1C). The serum levels of cardiac muscle troponin T (cTnT) and cTnI, two specific

biomarkers for ICI-myocarditis<sup>22</sup>, were induced in these mice (Supplementary Fig. 1D).

To explore the possible activation of pyroptosis in aPD-1-induced myocarditis, we determined the mRNA levels of four gasdermin family members (*Gsdma*, *Gsdmc*, *Gsdmd* and *Gsdme*) in mice. We found only *Gsdme* was induced by aPD-1 therapy (Fig. 1C). Meanwhile, the mRNA levels of *caspase-3*, *caspase-8* and *caspase-9*, but not the canonical pyroptosis-related caspases (*caspase-1* and *caspase-11*), were upregulated in aPD-1-treated mice heart (Supplementary Fig. 1E). At protein level, the cleavages of GSDME, caspase-3, caspase-8 and caspase-9, but not GSDMD, caspase-1 and caspase-11, were detected after aPD-1 treatment (Fig. 1D). At mRNA level, *Caspase-3* was induced earlier than *Gsdme*, while *Gsdme* mRNA maintained at a consistently high level throughout the entire administration period (Fig. 1E). By using flow cytometry in cells from aPD-1-treated mouse heart with propidium iodide (PI, a probe of cell death) and a specific antibody against N-terminal fragment of GSDME (referred as “GSDME-N”), which is the ‘real’ executor of GSDME-mediated pore formation in cell plasma membranes, we observed that the proportions of GSDME-N<sup>+</sup> cells were significantly enhanced (Fig. 1F). Interestingly, some GSDME-N<sup>+</sup> cells were also PI<sup>+</sup>, suggesting these cells underwent pyroptosis (Fig. 1F). Immunofluorescence staining of GSDME-N showed that myocardial GSDME-N was induced after aPD-1 therapy, and GSDME-N appeared to be localized along the outer contour of the cardiomyocytes (Fig. 1G). As GSDME was reported to pore on the mitochondrial membrane<sup>23</sup>, we observed the myocardial mitochondrion under transmission electron microscopy (TEM). The mitochondrial pores or penetrations (red arrows) were clearly noted in TEM analysis (Fig. 1H). The expressions of genes of myocarditis biomarkers (*Tnnt3* and *Tnnt2*), inflammatory factors (*Il-18*, *Il-6*, *Il-1 $\beta$* , *Ifn- $\gamma$*  and *Il-17 $\alpha$* ) and cell migration (*Icam1*, *Vav2* and *Sell*), were also significantly upregulated in aPD-1-treated mice heart tissue (Supplementary Fig. 1F). All these results indicate that aPD-1-therapy activated GSDME-dependent pyroptosis in mouse heart.

We sought to further decipher the involvement of GSDME-mediated pyroptosis in aPD-1-related myocarditis in human. We collected serum samples from six patients who were diagnosed with myocarditis according to International Society of Cardio-Oncology (IC-OS) 2021 Consensus<sup>24</sup> from total 360 tumor patients with one course of aPD-1 therapy (Fig. 1I), who were enrolled in a clinical trial conducted by our colleagues (No. NCT03239015) with the primary aim of evaluating the efficacy of targeted prevention therapy in patients with refractory tumors<sup>25,26</sup>. Serum from thirty age- and gender-matched tumor patients without myocarditis were used as





control. The clinical characteristics of the 6 patients with myocarditis were illustrated in Supplementary Table 1. Serum levels of ICI-associated myocarditis biomarkers, including cTnT, cTnI, CK-MB and NT-proB-type natriuretic peptide (NT-proBNP), were significantly increased post treatment in the 6 patients with myocarditis but not in those without myocarditis (Supplementary Fig. 2A, B). The numbers of circulating lymphocytes, monocytes and neutrophils were

enhanced in the 6 patients with myocarditis (Fig. 1J). Importantly, serum levels of GSDME were significantly induced in these patients (Fig. 1K). However, such changes in the number of circulating immune cells (Fig. 1L) and serum GSDME level (Fig. 1M) were not observed in the 30 tumor patients without myocarditis. These results suggest that GSDME-mediated pyroptosis may play a potential role in aPD-1-induced myocarditis in human.



**Fig. 2 | Deletion of GSDME alleviates aPD-1 therapy-induced myocarditis and mitochondrial damage.** **A** Morphology of hearts isolated from tumour-bearing WT and *Gsdme*<sup>-/-</sup> mice received aPD-1 therapy or control IgG. **B** Representative hematoxylin & eosin (H&E) staining and amplified images in whole heart section. The infiltrated immune cells were obviously noted in the myocardium of WT mice received aPD-1 therapy (blue dotted-line area). Scale bar, 200  $\mu$ m. **C** Representative echocardiograms and quantitative analyses of heart systolic functions, including left ventricular ejection fraction (LVEF), LV end systolic volume (LVESV) and LV end diastolic volume (LVEDV) in WT and *Gsdme*<sup>-/-</sup> mice received aPD-1 therapy or control IgG. **D** Running distance and time of WT and *Gsdme*<sup>-/-</sup> mice received aPD-1 therapy or control IgG. **E** Serum concentrations of cTnT, cTnI and CK-MB in WT and *Gsdme*<sup>-/-</sup> mice received aPD-1 therapy or control IgG. **F** The mRNA levels of *Tnnt2* (encoding cTnT) and *Tnni3* (encoding cTnI) in hearts of WT and *Gsdme*<sup>-/-</sup> mice

received aPD-1 therapy or control IgG. **G** Representative staining images of wheat germ agglutinin (WGA, for cardiomyocyte membrane labeling) in heart section and quantitative analysis of cardiomyocyte size in WT and *Gsdme*<sup>-/-</sup> mice received aPD-1 therapy or control IgG. DAPI (blue) was used to stain nuclei. Scale bar, 10  $\mu$ m. **H** Representative Sirius-Red staining in heart section and quantitative analysis of myocardial fibrosis in WT and *Gsdme*<sup>-/-</sup> mice received aPD-1 therapy or control IgG. The red-stained fiber is collagen fibers. Scale bar, 100  $\mu$ m. **I** Representative immunoblotting of IL-1 $\beta$  and its mature cleavage form in heart of WT and *Gsdme*<sup>-/-</sup> mice received aPD-1 therapy or normal IgG. **J** Representative transmission electron microscopy (TEM) images and quantitative analysis of mitochondrial damage in heart of WT and *Gsdme*<sup>-/-</sup> mice received aPD-1 therapy or control IgG. Scale bar, 5  $\mu$ m. The data were presented as means  $\pm$  SEM and analyzed by two-sided unpaired Student's t-tests.  $n = 6$  biologically independent experiments.

### Gsdme knockout mice are protected from aPD-1 therapy-induced myocarditis and mitochondrial damage

Next, we developed a mouse strain with global GSDME knockout (*Gsdme*<sup>-/-</sup>, Supplementary Fig. 3A–E) to determine the role of GSDME in overdose aPD-1 therapy-induced myocarditis. Deletion of *Gsdme* was confirmed at mRNA and protein levels (Supplementary Fig. 3F, G). Deletion of *Gsdme* did not alter the mRNA expression and enzymatic activities of caspases (Supplementary Fig. 3H, I). Tumour-bearing *Gsdme*<sup>-/-</sup> and their littermate WT control mice were challenged with aPD-1 therapy. Therapy of aPD-1 slightly but significantly decreased body weight in WT mice but not in *Gsdme*<sup>-/-</sup> mice (Supplementary Fig. 4A). After aPD-1 therapy, the WT mice demonstrated significance increases in heart weight/body weight (HW/BW) and heart weight/tibia length (HW/TL), which were partially reduced in *Gsdme*<sup>-/-</sup> mice (Supplementary Fig. 4B). The hearts of WT and *Gsdme*<sup>-/-</sup> mice were comparable in size in the absence of aPD-1 therapy; however, the size of heart was significantly enlarged in aPD-1-treated WT mice and, to a lesser extent in *Gsdme*<sup>-/-</sup> mice (Fig. 2A). In line with previous findings<sup>27,28</sup>, hematoxylin & eosin (H & E) staining on whole heart demonstrated that overdose aPD-1 administration induced dilated cardiomyopathy in WT mice but not *Gsdme*<sup>-/-</sup> mice (Fig. 2B). More importantly, there were massive infiltrated immune cells in the ventricular wall and interventricular septum of heart of aPD-1-treated WT mice but not *Gsdme*<sup>-/-</sup> mice (blue dotted-line area, Fig. 2B). Echocardiography showed that *Gsdme*<sup>-/-</sup> mice were resistant to aPD-1 therapy-induced harmful changes in systolic dysfunction (Fig. 2C). Exercise capacity related with myocardial function were also measured, and similar changes in running distance and time during exercise exhaustion test were observed (Fig. 2D). The aPD-1 therapy-induced enhancements of serum myocardial injury biomarkers (cTnT, cTnI and CK-MB) were attenuated in *Gsdme*<sup>-/-</sup> mice compared with WT mice (Fig. 2E). Accordingly, the increases in myocardial mRNA level of *Tnnt2* (encoding cTnT) and *Tnni3* (encoding cTnI) were inhibited in *Gsdme*<sup>-/-</sup> mice (Fig. 2F). Wheat germ agglutinin (WGA) staining demonstrated that the cardiomyocyte size was increased significantly by aPD-1 therapy in WT mice and, to a lesser extent in *Gsdme*<sup>-/-</sup> mice (Fig. 2G). Sirius-Red staining indicated an obvious accumulation of collagen in WT mice but not *Gsdme*<sup>-/-</sup> mice (Fig. 2H). Immunoblotting analysis of the pyroptosis-related inflammatory molecule IL-1 $\beta$  showed that the cleavage of IL-1 $\beta$  was blocked in *Gsdme*<sup>-/-</sup> mice (Fig. 2I). These results suggest that *Gsdme* knockout mice are protected from aPD-1 therapy-induced myocarditis.

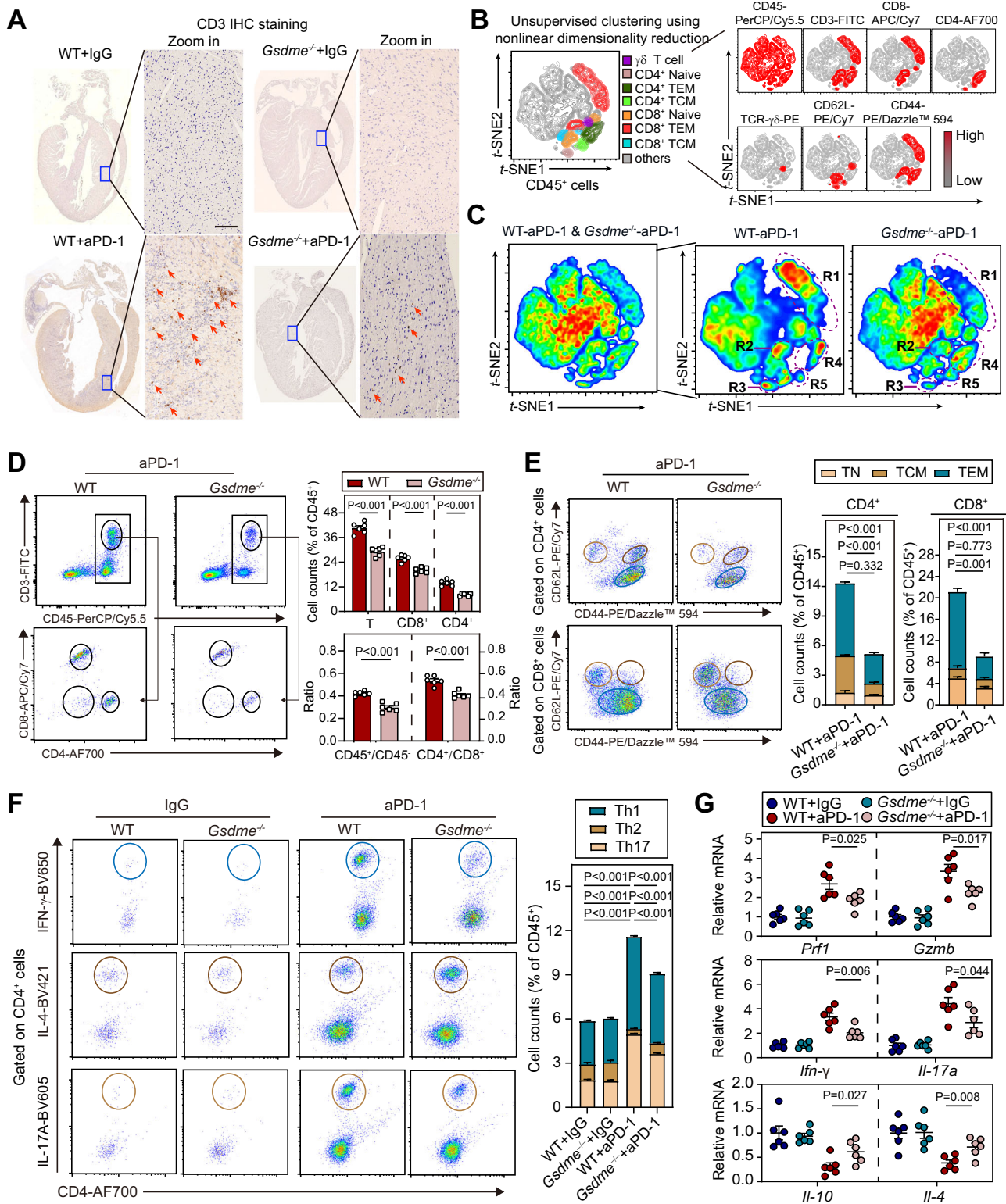
We also evaluated the mitochondrial damage in heart tissue. Transmission electron microscopy (TEM) analysis showed there were numerous broken mitochondria in heart tissue of aPD-1-treated WT mice and, to a lesser extent in *Gsdme*<sup>-/-</sup> mice (Fig. 2J), suggesting the mitochondrial integrity was protected by *Gsdme* deletion. In line with this, the induction of cytosolic mitochondrial DNA (mtDNA), including *mt-Nd1* and *D-loop* in aPD-1-treated WT mice heart and, to a lesser extent in *Gsdme*<sup>-/-</sup> deletion (Supplementary Fig. 4C). Flow cytometry

with mitoSOX probe, a specific dye for mitochondrial-specific reactive oxygen species (mt-ROS) demonstrated that aPD-1 treatment induced a significant increase of mito-ROS in WT mice heart and, to a much lesser extent in *Gsdme*<sup>-/-</sup> mice heart tissue (Supplementary Fig. 4D). The decreased myocardial activities of mitochondrial complex I and IV by aPD-1 treatment was partially blocked by GSDME deletion (Supplementary Fig. 4E). The mitochondrial levels of metabolic factors, including NAD<sup>+</sup>, ATP and glutathione (GSH), were decreased by aPD-1 treatment in WT mice heart, which were partially rescued in *Gsdme*<sup>-/-</sup> mice heart (Supplementary Fig. 4F). All these results suggest that GSDME-mediated pyroptosis is required for the aPD-1-induced cardiac dysfunction and mitochondrial damage.

### Gsdme<sup>-/-</sup> mice are protected from aPD-1 therapy-induced activation and cardiac infiltration of T-cell

As myocardial infiltration of T-cells is a key feature of ICI-associated cardiac irAEs<sup>29,30</sup>, we evaluated the T-cell activation and cardiac infiltration in our model. Immunohistochemistry of CD3 showed that there were plenty of T-cells within the myocardium of aPD-1-treated WT mice but, to a lesser extent in *Gsdme*<sup>-/-</sup> mice (Fig. 3A). We used multiplexed flow cytometry to further characterize the infiltrated T-cells in hearts. CD45<sup>+</sup> single cells isolated from aPD-1-treated mice heart were stained with antibodies against CD3, CD4, CD8, TCR- $\gamma\delta$ , CD62L and CD44, and then analyzed using an unsupervised clustering using nonlinear dimensionality reduction approach (Fig. 3B). With t-distributed stochastic neighbor embedding (t-SNE)-guided gating based on the markers, several T-cell clusters, including  $\gamma\delta$  T, CD8<sup>+</sup> Naïve T, CD8<sup>+</sup> T effector memory (TEM), CD8<sup>+</sup> T central memory (TCM), CD4<sup>+</sup> Naïve T, CD4<sup>+</sup> TEM and CD4<sup>+</sup> TCM, were identified (Fig. 3B). In the t-SNE heatmap (Fig. 3C), the aPD-1-treated *Gsdme*<sup>-/-</sup> mice had significantly lowered proportions of CD8<sup>+</sup> TEM (region 1 + 2, referred as R1 + R2) and CD4<sup>+</sup> Naïve T-cells (R3), as well as increased proportions of CD4<sup>+</sup> TEM (R4) and TCM (R5), compared with aPD-1-treated WT mice.

The influence of *Gsdme* deletion on myocardial T-cells populations was further evaluated by flow cytometry with conventional manual gating (see gating strategy in Supplementary Fig. 5). The proportions of total T cells, CD4<sup>+</sup> T and CD8<sup>+</sup> T, as well as CD4<sup>+</sup>/CD8<sup>+</sup> ratio, were significantly reduced in aPD-1-treated *Gsdme*<sup>-/-</sup> mice relative to WT mice (Fig. 3D). Among the CD4<sup>+</sup> T-cells, the proportions of CD4<sup>+</sup> TEM and CD4<sup>+</sup> TCM were significantly decreased, while the proportion of CD4<sup>+</sup> Naïve T (TN) was not changed (Fig. 3E). Among the CD8<sup>+</sup> T-cells, the proportions of CD8<sup>+</sup> TN and CD8<sup>+</sup> TEM were also significantly decreased, while the proportion of CD8<sup>+</sup> TCM was not changed (Fig. 3E). T-helper type 1 (Th1), T-helper type 2 (Th2) cells and T-helper 17 (Th17) cells were further identified based on IFN- $\gamma$ , IL-4 and IL-17A expression. In WT mice, aPD-1 treatment significantly increased proportions of Th1 and Th17 cells, and reduced proportion of Th2 cells; however, these changes induced by aPD-1 were weakened in *Gsdme*<sup>-/-</sup> mice (Fig. 3F). Accordingly, upon aPD-1 treatment, *Gsdme*<sup>-/-</sup> mice had lower gene expression of CD8<sup>+</sup> T or CD4<sup>+</sup> Th1-derived products (*Prfl*,



*Gzmb*, *Ifn- $\gamma$*  and *Il-17a*), as well as higher expression of CD4<sup>+</sup> Th2-derived products (*Il-10* and *Il-4*) compared with WT mice (Fig. 3G). We also evaluated the effects of *Gsdme* deletion on spleen T-cells populations. Treatment of aPD-1 induced a comparable weight-gain of spleen in WT and *Gsdme*<sup>-/-</sup> mice (Supplementary Fig. 6A). Immunohistochemistry staining showed that the aPD-1-induced increases of CD8<sup>+</sup> and CD4<sup>+</sup> T-cells in spleen were inhibited in *Gsdme*<sup>-/-</sup> mice (Supplementary Fig. 6B, C). The aPD-1-induced increases in proportions of Th1 and Th17 cells were also diminished in *Gsdme*<sup>-/-</sup> mice

(Supplementary Fig. 6D). Taken together, these findings indicate that global deletion of GSDME attenuates aPD-1 therapy-induced activation and cardiac infiltration of T-cell.

***Gsdme*<sup>-/-</sup> mice are protected from aPD-1 therapy-induced cardiac myeloid cells infiltration and inflammation**

Overactivation of innate immune myeloid cells is one of features for ICI-related myocarditis<sup>2,31</sup>. Thus, we investigated the effect of GSDME deletion on activation and cardiac infiltration of myeloid cells upon

**Fig. 3 | Deletion of GSDME attenuates aPD-1 therapy-induced activation and cardiac infiltration of T-cell.** **A** Infiltration of T-cells into myocardium was evaluated by immunohistochemistry staining of CD3 in WT and *Gsdme*<sup>-/-</sup> mice received aPD-1 therapy or control IgG. The images of whole heart section and amplified specific area were illustrated. Scale bar, 200 μm. **B** Unsupervised clustering using t-SNE nonlinear dimensionality reduction in CD45<sup>+</sup> cells with the CD3, CD4, CD8, TCR-γδ, CD62L and CD44 markers. The colors in the expression-level heatmaps (right panel) represent the median intensity values for each marker. **C** Relative clustering of heart T-cells from WT and *Gsdme*<sup>-/-</sup> mice. The significantly different regions 1 to 5 (R1-5) were circled. The cells in these regions were designated in (B). **D** Proportions of CD4<sup>+</sup> and CD8<sup>+</sup> T-cells within CD45<sup>+</sup> cells in hearts of WT and

*Gsdme*<sup>-/-</sup> mice were determined using flow cytometry analysis based on CD4 and CD8. **E** Proportions of T Naïve (TN), T effector memory (TEM), T central memory (TCM) cells within CD4<sup>+</sup> and CD8<sup>+</sup> T-cells in hearts of WT and *Gsdme*<sup>-/-</sup> mice were determined using flow cytometry analysis based on CD44 and CD62L. **F** Proportions of Th1 (IFN-γ<sup>+</sup>), Th2 (IL-4<sup>+</sup>) and Th17 (IL-17A<sup>+</sup>) cells in CD45<sup>+</sup> cells in hearts of WT and *Gsdme*<sup>-/-</sup> mice were determined using flow cytometry analysis. **G** The mRNA levels of CD8<sup>+</sup> and CD4<sup>+</sup> T-cell released cytotoxic molecules (*Pf1* and *Gzmb*), pro-inflammatory factors (*Ifn-γ* and *Il-17a*) and anti-inflammatory factors (*Il-10* and *Il-4*) in heart of WT and *Gsdme*<sup>-/-</sup> mice received aPD-1 therapy or control IgG. The data were presented as means ± SEM and analyzed by two-sided unpaired Student's t-tests. *n* = 6 biologically independent experiments.

aPD-1 therapy in our model. Immunohistochemistry of CD68 showed that there were numerous of infiltrated MOs/MPs in the myocardium of aPD-1-treated WT mice but, to a lesser extent in *Gsdme*<sup>-/-</sup> mice (Fig. 4A). Similarly, multiplexed flow cytometry was applied to characterize the infiltrated myeloid cells in hearts with antibodies against CD11b, Ly6G, F4/80, MHC-II, CCR2, Ly6C and CD64 using an unsupervised clustering (Fig. 4B). With t-SNE-guided automatic gating, several myeloid cells clusters, including MHC-II<sup>hi</sup> MPs, MHC-II<sup>lo</sup> MPs, Ly6C<sup>hi</sup> MOs, Ly6C<sup>lo</sup> MOs and Ly6G<sup>+</sup> neutrophils, were identified (Fig. 4B). In the heatmap (Fig. 4C), compared with aPD-1-treated WT mice, the aPD-1-treated *Gsdme*<sup>-/-</sup> mice had decreased proportions of MHC-II<sup>hi</sup> MPs (R1) and Ly6C<sup>hi</sup> MOs (R2), as well as increased proportion of Ly6C<sup>lo</sup> MOs (R3).

We further used manual gating to determine the influence of *Gsdme* deletion on myocardial MOs/MPs populations. The aPD-1-induced proportion of M1-like Mos/MPs (CD11b<sup>+</sup>CD64<sup>+</sup>) was pronouncedly reduced in *Gsdme*<sup>-/-</sup> mice (Fig. 4D). In line with this finding, there signature genes for M1-like Mos/MPs (*Nos2*, *H2-Dma* and *Axl*) were significantly triggered by aPD-1 treatment in WT mice but not in *Gsdme*<sup>-/-</sup> mice (Fig. 4E). In the MOs (CD45<sup>+</sup>CD11b<sup>+</sup>CD3<sup>-</sup>Ly6G<sup>-</sup>F4/80<sup>-</sup>), the proportion of pro-inflammatory Ly6C<sup>hi</sup> MOs increased while the proportion of anti-inflammatory Ly6C<sup>lo</sup> MOs decreased in response to aPD-1 (Fig. 4F), suggesting aPD-1 causes a shift of MOs towards Ly6C<sup>hi</sup> status. Nevertheless, both of these changes were inhibited in *Gsdme*<sup>-/-</sup> mice (Fig. 4F). As shown in Fig. 4G, the MPs (CD45<sup>+</sup>CD11b<sup>+</sup>CD3<sup>-</sup>Ly6G<sup>-</sup>F4/80<sup>-</sup>) were further characterized to three clusters: CCR2<sup>-</sup>MHC-II<sup>lo</sup> (local resident MPs without antigen processing/presentation action), CCR2<sup>-</sup>MHC-II<sup>hi</sup> (local resident MPs with antigen processing/presentation action) and CCR2<sup>+</sup>MHC-II<sup>hi</sup> (highly pro-inflammatory MPs derived from blood MOs through a CCR2-dependent mechanism). The proportion of CCR2<sup>-</sup>MHC-II<sup>lo</sup> MPs were reduced by aPD-1 in WT mice, which was reversed in *Gsdme*<sup>-/-</sup> mice (Fig. 4G). Both the proportions of CCR2<sup>-</sup>MHC-II<sup>hi</sup> and CCR2<sup>+</sup>MHC-II<sup>hi</sup> MPs were largely induced by aPD-1 in WT mice but to a lesser extent in *Gsdme*<sup>-/-</sup> mice (Fig. 4G). We also evaluated the infiltration of neutrophils, a crucial player in myocarditis<sup>32</sup>. The expression levels of myeloperoxidase (MPO) and C-X-C motif chemokine receptor 2 (CXCR2), two critical factors for neutrophils function, were triggered in WT mice heart and to lesser extents in *Gsdme*<sup>-/-</sup> mice heart (Supplementary Fig. 7A). Similar changes were observed in the mRNA levels of two neutrophils-related genes *Elane* and *Padi4* (Supplementary Fig. 7B). qPCR analyses of *Il-1β*, *Il-6*, *Il-18* and *Il-2* demonstrated these pro-inflammatory factors were induced in WT mice heart upon aPD-1 therapy, which were remarkably attenuated in *Gsdme*<sup>-/-</sup> mice (Supplementary Fig. 7C). These indicate that global deletion of GSDME alleviates aPD-1 therapy-induced cardiac myeloid cell infiltration and inflammation.

### Deficiency of *Gsdme* ameliorates myocarditis in *Pdcd1*<sup>-/-</sup> receiving anti-Ctla4 treatment

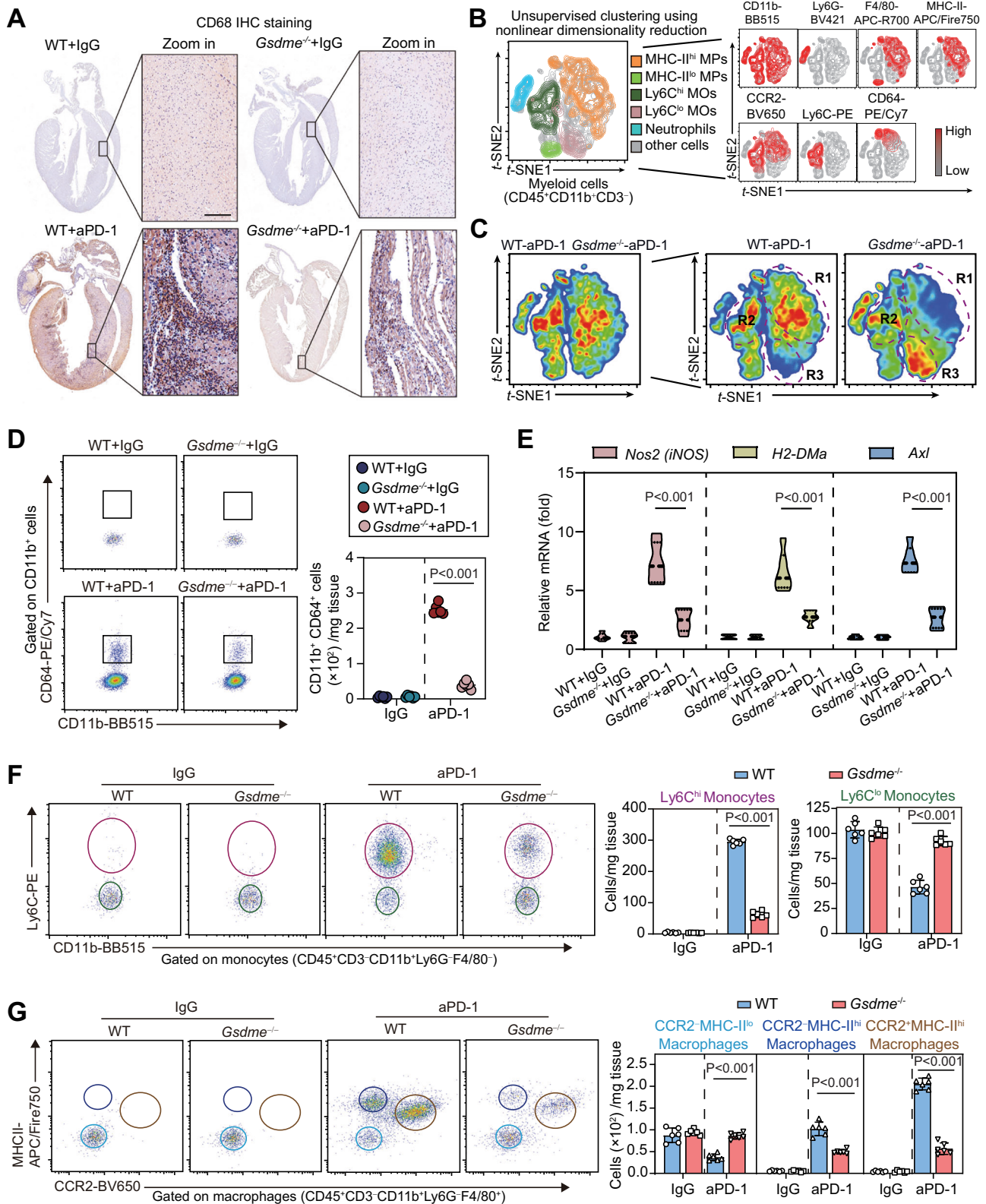
In clinical practice, it has been observed that combined therapy with anti-PD1 and anti-CTLA4 in advanced cancer patients is associated with

a higher incidence of ICI-induced myocarditis<sup>33,34</sup>. Additionally, studies in mice have shown that combined inhibition or simultaneous deletion of PD-1 and CTLA4 replicates pronounced ICI-induced myocarditis without additional interventions such as tumor<sup>7,8,35,36</sup>. Taking these findings into consideration, we employed the second animal model of ICI-induced myocarditis involving combined inhibition of PD-1 and CTLA-4 without tumor to validate our aforementioned observations in tumor-bearing mice treated with aPD-1 alone. We generated PD-1/GSDME double knockout mice (*Pdcd1*<sup>-/-</sup>*Gsdme*<sup>-/-</sup>), which simultaneously lack PD-1 and GSDME proteins systemically. *Pdcd1*<sup>-/-</sup>*Gsdme*<sup>-/-</sup> mice and *Pdcd1*<sup>-/-</sup> mice were then treated with an antibody against CTLA4 to achieve combined inhibition of PD-1 and CTLA4 (Fig. 5A). Histological analysis revealed that the number of infiltrated immune cells in the hearts of anti-Ctla4-treated *Pdcd1*<sup>-/-</sup>*Gsdme*<sup>-/-</sup> mice was significantly lower than that in anti-Ctla4-treated *Pdcd1*<sup>-/-</sup> mice (Fig. 5B). Immunohistochemical staining also demonstrated that the numbers of cardiac CD4<sup>+</sup> T cells and CD8<sup>+</sup> T cells in anti-Ctla4-treated *Pdcd1*<sup>-/-</sup>*Gsdme*<sup>-/-</sup> mice were lower than those in anti-Ctla4-treated *Pdcd1*<sup>-/-</sup> mice (Fig. 5C). Utilizing multiplexed flow cytometry with t-SNE-guided automatic gating, T-cell subclusters, including γδ T, CD8<sup>+</sup> Naïve T, CD8<sup>+</sup> TEM, CD8<sup>+</sup> TCM, CD4<sup>+</sup> Naïve T, CD4<sup>+</sup> TEM, and CD4<sup>+</sup> TCM, were identified (Fig. 5D). In the t-SNE heatmap, anti-Ctla4-treated *Pdcd1*<sup>-/-</sup>*Gsdme*<sup>-/-</sup> mice exhibited significantly increased proportions of CD4<sup>+</sup> Naïve T (R1) and CD8<sup>+</sup> Naïve T (R2), as well as reduced proportions of CD8<sup>+</sup> TEM (R3), CD4<sup>+</sup> TEM (R4), and CD4<sup>+</sup> TCM (R5), compared with anti-Ctla4-treated *Pdcd1*<sup>-/-</sup> mice (Fig. 5E). Flow cytometry with manual gating also demonstrated that the numbers of CD4<sup>+</sup> T and CD8<sup>+</sup> T cells were lower in the hearts of *Pdcd1*<sup>-/-</sup>*Gsdme*<sup>-/-</sup> mice than those of *Pdcd1*<sup>-/-</sup> mice (Fig. 5F, G).

Myeloid cell subclusters were also identified using multiplexed flow cytometry with t-SNE-guided automatic gating. MHC-II<sup>hi</sup> MPs, MHC-II<sup>lo</sup> MPs, Ly6C<sup>lo</sup> MOs, Ly6C<sup>hi</sup> MOs, and neutrophils, were identified (Fig. 6A). In the t-SNE heatmap, anti-Ctla4-treated *Pdcd1*<sup>-/-</sup>*Gsdme*<sup>-/-</sup> mice had significantly reduced proportions of MHC-II<sup>hi</sup> MPs (R1) and Ly6C<sup>hi</sup> MOs (R2), as well as increased proportions of MHC-II<sup>lo</sup> MPs (R3) and Ly6C<sup>lo</sup> MOs (R4), compared with anti-Ctla4-treated *Pdcd1*<sup>-/-</sup> mice (Fig. 6B). Flow cytometry with manual gating revealed that the number of NOS2<sup>+</sup> M1-like MPs/MOs was reduced in the hearts of anti-Ctla4-treated *Pdcd1*<sup>-/-</sup>*Gsdme*<sup>-/-</sup> mice compared with anti-Ctla4-treated *Pdcd1*<sup>-/-</sup> mice (Fig. 6C). Accordingly, the number of Ly6C<sup>hi</sup> MOs was decreased, while the number of Ly6C<sup>lo</sup> MOs was increased (Fig. 6D). Immunohistochemical staining of CD68 confirmed the inhibited infiltration of MPs/MOs in the heart of *Pdcd1*<sup>-/-</sup>*Gsdme*<sup>-/-</sup> mice (Fig. 6E). These results suggest that deficiency of *Gsdme* ameliorates myocarditis in *Pdcd1*<sup>-/-</sup> mice receiving anti-Ctla4 treatment.

Finally, we monitored whether systemic immune activation occurred in the two animal models of ICI-induced myocarditis. We observed that the mRNA levels of pro-inflammatory factors in peripheral blood mononuclear cells (PBMCs) were not enhanced in both models (Supplementary Fig. 8A, B). Moreover, we examined immune cell infiltration/immune response in various other organs, including





the diaphragm, skeletal muscle (quadriceps femoris muscle), lung, liver, and intestine, using histological analysis and qPCR. Notably, except for a very mild inflammation observed in the diaphragm of anti-Ctla4-treated *Pdcd1*<sup>-/-</sup> mice (Supplementary Fig. 8C, D), we did not observe obvious immune cell infiltration in other organs in the two mouse models (Supplementary Fig. 8E).

**GSDME in cardiomyocyte rather than myeloid cell is required for aPD-1 therapy-induced cardiac dysfunction and mitochondrial damage**

To decipher which type of cells in heart tissue process the GSDME-mediated pyroptosis in response to ICI, we isolated CD45<sup>+</sup> and CD45<sup>-</sup> cells from heart tissue of aPD-1-treated mice using sorting flow

**Fig. 4 | Deletion of GSDME reduces aPD-1 therapy-induced myeloid cell activation and cardiac infiltration.** **A** Infiltration of monocytes/macrophages (MOs/MPs) into myocardium was evaluated by immunohistochemistry staining of CD68 in WT and *Gsdme*<sup>-/-</sup> mice received aPD-1 therapy or control IgG. The images of whole heart section and amplified specific area were illustrated. Scale bar, 200  $\mu$ m. **B** Unsupervised clustering using t-SNE nonlinear dimensionality reduction in myeloid cells (CD45<sup>+</sup>CD11b<sup>+</sup>CD3<sup>-</sup>) cells with the CD11b, Ly6G, F4/80, MHC-II, CCR2, Ly6C and CD64 markers. The colors in the expression-level heatmaps (right panel) represent the median intensity values for each marker. **C** Subclusters of heart myeloid cells from WT and *Gsdme*<sup>-/-</sup> mice. The significantly different regions 1 to 3 (R1-3) were circled. The cells in these regions were designated in **(B)**. **D** Numbers of

MI-like MOs/MPs (CD11b<sup>+</sup>CD64<sup>+</sup>) in heart tissue of WT and *Gsdme*<sup>-/-</sup> mice were determined using flow cytometry analysis based on CD11b and CD64. **E** The mRNA expression of pro-inflammatory MOs/MPs-related genes (*Nos2*, *H2-DMA* and *Axl*) in heart tissue of WT and *Gsdme*<sup>-/-</sup> mice. **(F)** Numbers of Ly6C<sup>high</sup> (Ly6C<sup>hi</sup>) and Ly6C<sup>low</sup> (Ly6C<sup>lo</sup>) monocytes in heart tissue of WT and *Gsdme*<sup>-/-</sup> mice were determined using flow cytometry analysis. **G** Numbers of CCR2<sup>+</sup>MHC-II<sup>lo</sup>, CCR2<sup>+</sup>MHC-II<sup>hi</sup> and CCR2<sup>+</sup>MHC-II<sup>hi</sup> macrophages in heart tissue of WT and *Gsdme*<sup>-/-</sup> mice were determined using flow cytometry analysis. The data were presented as means  $\pm$  SEM and analyzed by two-sided unpaired Student's t-tests. *n* = 6 biologically independent experiments.

cytometry. The CD45<sup>-</sup> cells highly expressed *Myh6* (encoding cardiac  $\alpha$ -myosin heavy chain), whereas the CD45<sup>+</sup> cells highly expressed *Ptprc* (encoding CD45, Supplementary Fig. 9A). We found *Il-18* and *Il-1 $\beta$*  expressions were downregulated in CD45<sup>-</sup> cells but not CD45<sup>+</sup> cells of *Gsdme*<sup>-/-</sup> mice (Supplementary Fig. 9B). Moreover, *Il-18* gene expression was induced in CD45<sup>-</sup> cells, while *Ccr2* gene expression was induced in CD45<sup>+</sup> cells during the whole course of disease (Supplementary Fig. 9C). These results suggest that the pyroptosis process may occur in CD45<sup>-</sup> cells, which are mainly composed of cardiomyocytes.

To confirm this speculation, we analyzed two public single-cell RNA sequencing datasets (GEO Access Numbers: GSE162959 and GSE232466) in mouse heart using Uniform Manifold Approximation and Projection (UMAP) dimension reduction (Supplementary Fig. 10A, C). In the first scRNA-seq (GSE162959), *Gsdme*, but not the canonical pyroptosis mediator *Gsdmd*, was abundantly expressed in heart, especially in cardiomyocytes and fibroblasts (dotted line region, Supplementary Fig. 10B). In the second scRNA-seq dataset, *Gsdme* was enriched in cardiomyocytes and fibroblasts (black dotted line region), as well as immune cells such as macrophages, granulocytes, and T cells (red dotted line region); however, *Gsdmd* was mainly expressed in immune cells (Supplementary Fig. 10D). To know the type of immune cell mainly expresses *GSDME* gene, we additionally included a scRNA-seq on peripheral blood mononuclear cells (PBMCs) from patients with ICI-myocarditis (GEO Access Number: GSE180045, Supplementary Fig. 10E). In these immune cells, *GSDME* was found to be mainly expressed in MOs/MPs, but not T cells and NK cells (Supplementary Fig. 10F, G). These results not only support the previous notion that unlike *Gsdmd*, *Gsdme* is abundantly expressed in normal cells<sup>17</sup>, but also indicate that the cardiomyocytes and myeloid cells might be the major source of pyroptosis during ICI-myocarditis due to their high expression of *Gsdme*.

Next, we generated a mouse model carrying a transcriptional *Stop* element (3 $\times$ SV40-Poly A) flanked by *loxP* recombination sites (*loxP-Stop-loxP*, LSL)<sup>37</sup> upstream of the ATG start codon of *Gsdme* gene, which terminates transcription of *Gsdme* gene (Supplementary Fig. 11A–E). The *Gsdme*<sup>Stop/Stop</sup> mouse strain was crossed with *Myh6-Cre* or *Lysm-Cre* mouse to produce *Gsdme*<sup>Stop/Stop</sup>;*Myh6-Cre* mouse (cardiomyocyte rescue of GSDME, referred as *Gsdme*<sup>CR</sup>) or *Gsdme*<sup>Stop/Stop</sup>;*Lysm-Cre* mouse (myeloid cell rescue of GSDME, referred as *Gsdme*<sup>MR</sup>) for further investigation (Supplementary Fig. 11F). The tissue-specific rescue of GSDME in *Gsdme*<sup>CR</sup> and *Gsdme*<sup>MR</sup> mice were confirmed at mRNA and protein levels (Supplementary Fig. 11G, H).

The tumour-bearing WT, *Gsdme*<sup>Stop/Stop</sup>, *Gsdme*<sup>CR</sup> and *Gsdme*<sup>MR</sup> mice were challenged with aPD-1 therapy or control IgG. There were no significant differences in morphology and cardiac functions among the four stains under normal IgG treatment (Supplementary Fig. 12A–C). Therefore, we mainly compared their pathologies under aPD-1-treatment condition. *Gsdme*<sup>Stop/Stop</sup> mice had smaller size of heart compared with WT mice in response to aPD-1 administration; *Gsdme*<sup>CR</sup> mice, but not *Gsdme*<sup>MR</sup> mice, replicated the myocardial enlargement (Fig. 7A). H & E staining on whole heart clearly showed that the aPD-1

administration induced massive infiltration of immune cells in myocardium of WT and *Gsdme*<sup>CR</sup> mice (blue dotted-line area), but not *Gsdme*<sup>Stop/Stop</sup> and *Gsdme*<sup>MR</sup> mice (Fig. 7B). As expected, echocardiography showed that *Gsdme*<sup>Stop/Stop</sup> and *Gsdme*<sup>MR</sup> mice were resistant to aPD-1 therapy-induced cardiac malfunction (Fig. 7C). Exercise exhaustion test confirmed the improvement in cardiac function in *Gsdme*<sup>Stop/Stop</sup> and *Gsdme*<sup>MR</sup> mice, but not *Gsdme*<sup>CR</sup> mice (Fig. 7D). Accordingly, *Gsdme*<sup>CR</sup> mice, but not *Gsdme*<sup>Stop/Stop</sup> or *Gsdme*<sup>MR</sup> mice, displayed similar serum cTnl concentrations upon aPD-1 therapy to WT mice (Fig. 7E). This change was confirmed by the results of myocardial *Tnnt2* and *Tnni3* mRNA expression (Fig. 7F). WGA and Sirius-Red staining demonstrated that *Gsdme*<sup>CR</sup> mice, but not *Gsdme*<sup>MR</sup> mice, had significant aggravated cardiomyocyte hypertrophy and fibrosis than *Gsdme*<sup>Stop/Stop</sup> mice (Fig. 7G, H). The mRNA levels of fibrosis-related factors ( $\alpha$ -SMA, *Col1a1* and *Col3a1*) showed similar changes (Fig. 7I). The induced cytosolic mtDNA (*mt-Nd1*) in heart tissue were inhibited in *Gsdme*<sup>Stop/Stop</sup> mice compared with WT mice, while *Gsdme*<sup>CR</sup> mice but not *Gsdme*<sup>MR</sup> mice showed a remarkable restoration (Fig. 7J). Similarly, the mitochondrial complex I activity was rescued in *Gsdme*<sup>Stop/Stop</sup> and *Gsdme*<sup>MR</sup> mice but not in *Gsdme*<sup>CR</sup> mice (Fig. 7K). All these suggest that restoration of GSDME expression in cardiomyocytes but not myeloid cells in *Gsdme*-deficient mice, replicates aPD-1 therapy-induced myocarditis.

### GSDME in cardiomyocyte promotes immune cells infiltration and inflames the heart upon aPD-1 therapy

To better define the myocardial inflammation profile, we next examined whether the infiltration of immune cells was regulated by *Gsdme* in cardiomyocytes. Upon aPD-1 therapy, *Gsdme*<sup>Stop/Stop</sup> and *Gsdme*<sup>MR</sup> mice had decreased, whereas *Gsdme*<sup>CR</sup> mice had similar frequencies of CD8<sup>+</sup> and CD4<sup>+</sup> T-cells in heart compared with WT mice (Fig. 8A). Flow cytometry revealed similar results (Fig. 8B). The numbers or frequencies of pro-inflammatory Th1 and Th17 cells were decreased in *Gsdme*<sup>Stop/Stop</sup> and *Gsdme*<sup>MR</sup> mice, but not in *Gsdme*<sup>CR</sup> mice (Fig. 8C). The number or frequency of anti-inflammatory Th2 cells showed a reverse pattern (Fig. 8C). Th1 or Th17-derived products (*Ifn- $\gamma$* , *Tnf- $\alpha$* , *Il-22* and *Il-17a*) and Th2-derived products (*Il-4* and *Il-10*) displayed consistent trends (Supplementary Fig. 13A). Immunofluorescent analysis showed GSDME-N signal was detected in WT and *Gsdme*<sup>CR</sup> mice but not *Gsdme*<sup>Stop/Stop</sup> and *Gsdme*<sup>MR</sup> mice (Fig. 8D), suggesting that the *Gsdme*<sup>MR</sup> mice, which had a restricted rescue of GSDME in myeloid cells, did not undergo cardiac pyroptosis. Interestingly, the IFN- $\gamma$  signals did not colocalize GSDME-N signals (Fig. 8D), supporting that the GSDME cleavage was not happened in immune cells.

Fluorescent immunohistochemical analysis and flow cytometry demonstrated that the MOs/MPs infiltration was inhibited in *Gsdme*<sup>Stop/Stop</sup> and *Gsdme*<sup>MR</sup> mice but not in *Gsdme*<sup>CR</sup> mice (Fig. 8E and Supplementary Fig. 13B). *Gsdme*<sup>Stop/Stop</sup> and *Gsdme*<sup>MR</sup> mice, rather than *Gsdme*<sup>CR</sup> mice, had lower numbers of Ly6C<sup>hi</sup> and higher numbers of Ly6C<sup>lo</sup> monocytes compared with WT mice (Fig. 8F), suggesting inflammation was re-triggered only in *Gsdme*<sup>CR</sup> mice. Similar changes in myocardial numbers of CCR2<sup>+</sup>MHC-II<sup>low</sup>, CCR2<sup>+</sup>MHC-II<sup>high</sup> and



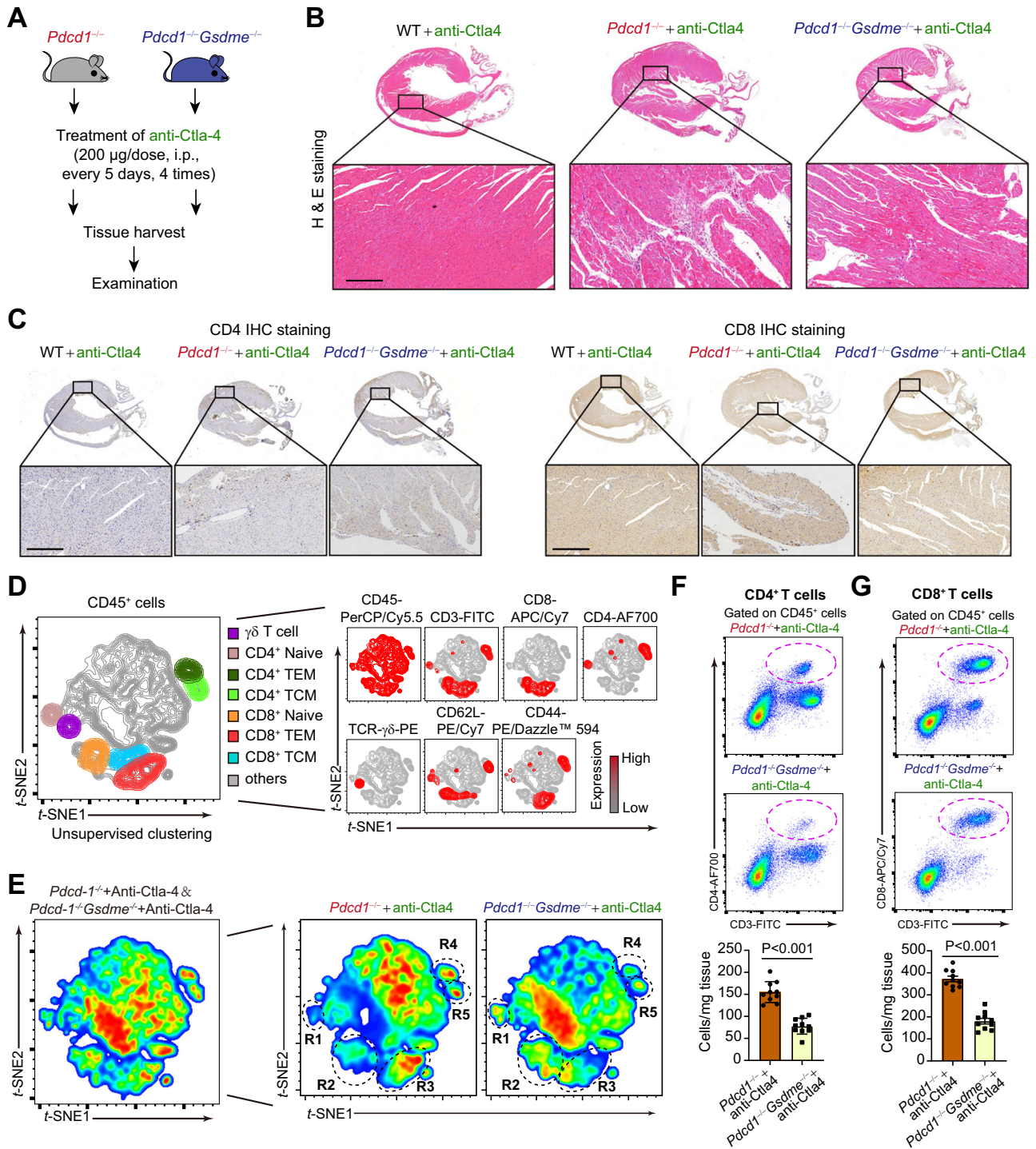
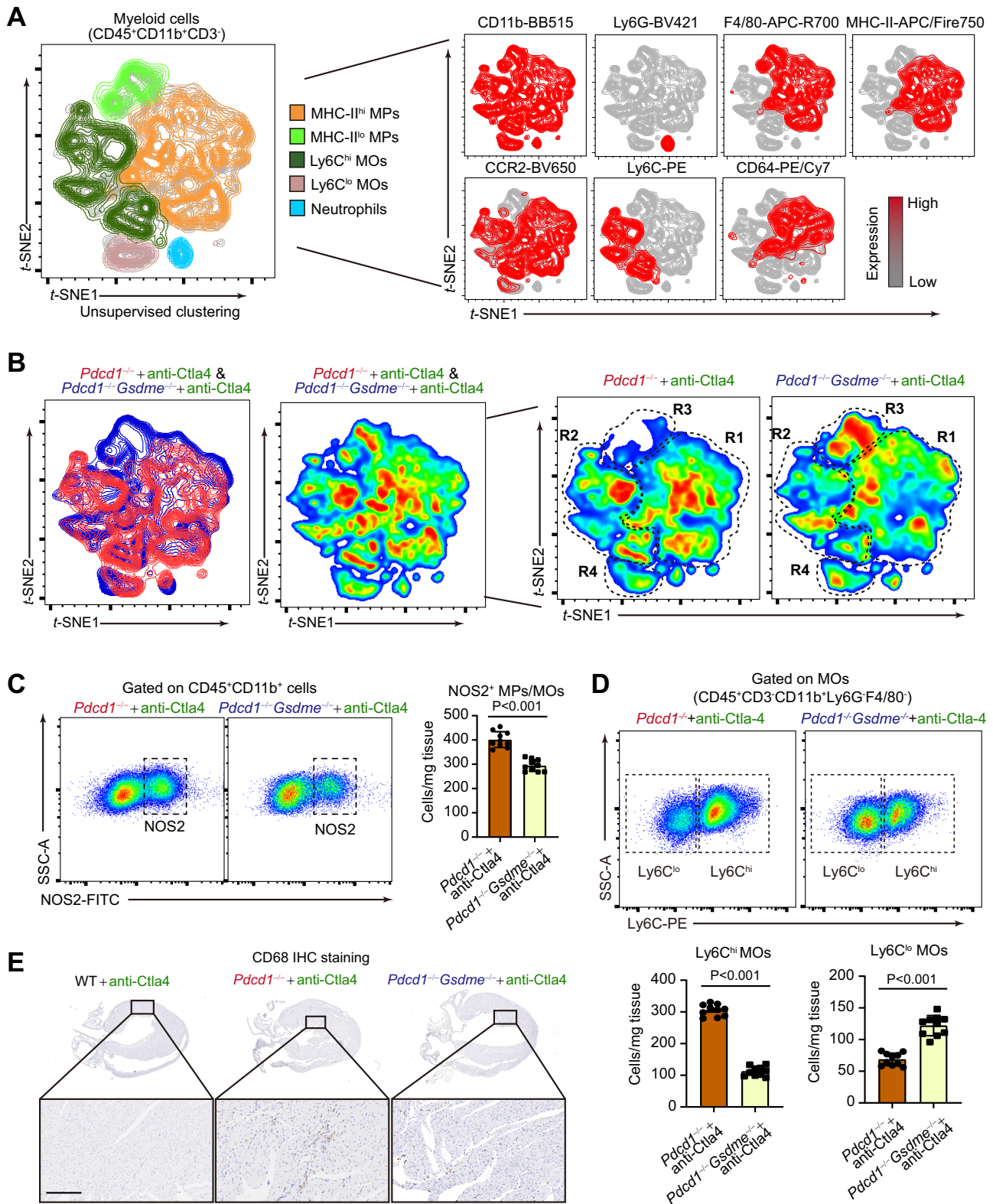


**Fig. 5 | Differences in T cells infiltration in hearts of *Pdc1*<sup>-/-</sup> and *Pdc1*<sup>-/-</sup>*Gsdme*<sup>-/-</sup> mice receiving anti-Ctla4 treatment.** **A** Experimental protocol for mouse model of myocarditis in *Pdc1*<sup>-/-</sup> mice and *Pdc1*<sup>-/-</sup>*Gsdme*<sup>-/-</sup> mice receiving treatment of anti-Ctla4. **B** Representative hematoxylin & eosin (H&E) staining and amplified images in whole heart section. The infiltrated immune cells were obviously noted in the myocardium of *Pdc1*<sup>-/-</sup> mice and *Pdc1*<sup>-/-</sup>*Gsdme*<sup>-/-</sup> mice receiving treatment of anti-Ctla4. Scale bar, 200  $\mu$ m. **C** Infiltration of T-cells into myocardium was evaluated by immunohistochemistry staining of CD4 and CD8 in the myocardium of *Pdc1*<sup>-/-</sup> mice and *Pdc1*<sup>-/-</sup>*Gsdme*<sup>-/-</sup> mice receiving treatment of anti-Ctla4. The images of whole heart section and amplified specific area were illustrated. Scale bar, 200  $\mu$ m. **D** Unsupervised clustering using t-SNE nonlinear dimensionality reduction in CD45<sup>+</sup> cells with the CD3, CD4, CD8, TCR- $\gamma\delta$ , CD62L and CD44 markers. The colors in the

expression-level heatmaps (right panel) represent the median intensity values for each marker. **E** Heatmap plot showing the different clusters of myocardial infiltrated T-cells between *Pdc1*<sup>-/-</sup> mice and *Pdc1*<sup>-/-</sup>*Gsdme*<sup>-/-</sup> mice receiving treatment of anti-Ctla4. The significantly different regions 1 to 5 (referred as R1-R5) were circled. The cells in these regions were designated in **(D)**. **F** Numbers of CD4<sup>+</sup> T-cells within CD45<sup>+</sup> cells in hearts of *Pdc1*<sup>-/-</sup> mice and *Pdc1*<sup>-/-</sup>*Gsdme*<sup>-/-</sup> mice receiving treatment of anti-Ctla4 were determined using flow cytometry analysis based on CD4. **G** Numbers of CD8<sup>+</sup> T-cells within CD45<sup>+</sup> cells in hearts of *Pdc1*<sup>-/-</sup> mice and *Pdc1*<sup>-/-</sup>*Gsdme*<sup>-/-</sup> mice receiving treatment of anti-Ctla4 were determined using flow cytometry analysis based on CD8. The data were presented as means  $\pm$  SEM and analyzed by two-sided unpaired Student's t-tests.  $n = 10$  biologically independent experiments.





CCR2<sup>+</sup>MHC-II<sup>high</sup> macrophages were observed in *Gsdme*<sup>CR</sup> mice heart (Fig. 8G), suggesting that antigen processing/presentation and migration of MOs/MPs induced by aPD-1 therapy were recovered in *Gsdme*<sup>CR</sup> mice heart tissue. In agreement with these results, *Gsdme*<sup>CR</sup> mice exhibited higher levels of myocardial pro-inflammatory factors (IL-1 $\beta$ , IL-18 and IL-6) and chemokine gene expression (*Ccr5* and *Ccl5*) compared with *Gsdme*<sup>Stop/Stop</sup> and *Gsdme*<sup>MR</sup> mice (Supplementary Fig. 13C, D). Taken together, these data suggest that the GSDME in

cardiomyocyte, but not myeloid cells, is decisive for the aPD-1 therapy-induced myocardial immune/inflammation activation.

**cGAS-STING signalling contributes to GSDME-mediated pyroptosis and myocarditis upon aPD-1 therapy**

To further understand the molecular mechanisms underlying the GSDME-mediated pyroptosis upon aPD-1 therapy, we used an isobaric Tandem Mass Tag (TMT)-based multiplexed quantitative proteomic

**Fig. 6 | Differences in myeloid cells infiltration in hearts of *Pdcd1*<sup>-/-</sup> and *Pdcd1*<sup>-/-</sup> *Gsdme*<sup>-/-</sup> mice receiving anti-Ctla4 treatment.** **A** Unsupervised clustering using t-SNE nonlinear dimensionality reduction in myeloid cells (CD45<sup>+</sup>CD11b<sup>+</sup>CD3<sup>-</sup>) cells with the CD11b, Ly6G, F4/80, MHC-II, CCR2, Ly6C and CD64 markers. The colors in the expression-level heatmaps (right panel) represent the median intensity values for each marker. **B** Heatmap plot showing the different clusters of myocardial infiltrated myeloid cells between *Pdcd1*<sup>-/-</sup> mice and *Pdcd1*<sup>-/-</sup> *Gsdme*<sup>-/-</sup> mice receiving treatment of anti-Ctla4. The significantly different regions 1 to 4 (referred as R1-R4) were circled. The cells in these regions were designated in **(A)**. **C** Numbers of NOS2<sup>+</sup> MI-like MPs/MOs within myeloid cells (CD45<sup>+</sup>CD11b<sup>+</sup>) in hearts of *Pdcd1*<sup>-/-</sup> mice and

*Pdcd1*<sup>-/-</sup> *Gsdme*<sup>-/-</sup> mice receiving treatment of anti-Ctla4 were determined using flow cytometry analysis based on NOS2. **D** Numbers of Ly6C<sup>hi</sup> and Ly6C<sup>low</sup> MOs within MOs (CD45<sup>+</sup>CD3<sup>+</sup>CD11b<sup>+</sup>Ly6G<sup>+</sup>F4/80<sup>-</sup>) in hearts of *Pdcd1*<sup>-/-</sup> mice and *Pdcd1*<sup>-/-</sup> *Gsdme*<sup>-/-</sup> mice receiving treatment of anti-Ctla4 were determined using flow cytometry analysis based on Ly6C staining. **E** Infiltration of MPs/MOs into myocardium was evaluated by immunohistochemistry staining of CD68 in the myocardium of *Pdcd1*<sup>-/-</sup> mice and *Pdcd1*<sup>-/-</sup> *Gsdme*<sup>-/-</sup> mice receiving treatment of anti-Ctla4. The images of whole heart section and amplified specific area were illustrated. Scale bar, 200 μm. The data were presented as means ± SEM and analyzed by two-sided unpaired Student's t-tests. *n* = 10 biologically independent experiments.

technique to analyze differentially-expressed proteins (DEPs) of *Gsdme*<sup>-/-</sup> mice compared with WT mice upon aPD-1 therapy (Fig. 9A). By this strategy, we identified 112 DEPs (fold change >1.2 or <0.83, *P*-value <0.05), including 58 downregulated and 54 upregulated proteins (Fig. 9B and Supplementary Table 2). The top 20 downregulated and upregulated proteins were shown in Fig. 9C. Protein-protein-interaction mapping (PPI) analysis of the DEPs highlighted a network of IFN-related proteins (Fig. 9D). Kyoto Encyclopedia of Genes and Genomes (KEGG) analysis revealed that the DEPs were mainly associated with antigen processing/presentation, cytokine release, IFN signaling and mitochondria integrity regulation (Fig. 9E). Gene Ontology (GO) analysis also showed that the DEPs were mainly associated with immune system process, antigen processing/presentation, T-cell mediated cytotoxicity and IFN signaling (Fig. 9F). In line with these results, *Gsdme*<sup>-/-</sup> mice exerted comprehensive inhibited protein signatures in immune cells in heart tissue upon aPD-1 therapy (Supplementary Fig. 14A–F). Interestingly, the fibroblast-related protein signature was also reduced in *Gsdme*<sup>-/-</sup> mice heart upon aPD-1 therapy (Supplementary Fig. 14G). These proteomic results suggest that *Gsdme* deletion is highly linked to IFN signaling and mitochondrial during aPD-1 induced myocarditis.

Based on the proteomics results, we proposed that the cGAS-STING pathway, which links IFN signal and immune by sensing exogenous DNA<sup>38</sup>, might be involved in the action of GSDME. As expected, the induced plasma levels of mtDNA and double-stranded DNA (dsDNA) by aPD-1 treatment were partially suppressed in *Gsdme*<sup>-/-</sup> mice (Fig. 9G, H). Thus, we turned to scrutinize the importance of cGAS-STING pathway in aPD-1 therapy-induced cardiac damage. Upon aPD-1 therapy, the protein expression of cGAS, STING, phospho-TBK1 (p-TBK1), phospho-IRF3 (p-IRF3) and total-IRF3 were up-regulated in WT mice heart (Fig. 9I). However, these changes were apparently attenuated in *Gsdme*<sup>-/-</sup> mice. These suggest that cGAS-STING signalling is regulated by GSDME-mediated pyroptosis and may be a key mediator of aPD-1 therapy-induced cardiac damage. We also used a mouse strain with global STING deficiency (golden-ticket mutant, *Sting*<sup>gt/gt</sup>) to ascertain the essential role of cGAS-STING signalling in aPD-1 therapy-induced cardiac damage. Echocardiography analysis showed that *Sting*<sup>gt/gt</sup> mice were protected from aPD-1 therapy-induced cardiac dysfunction compared with WT mice (Fig. 9J). Notably, the aPD-1 therapy-induced elevations in serum cTnT and cTnI concentrations (Fig. 9K), cleavage of GSDME (Fig. 9L), and myocardial infiltration of both CD4<sup>+</sup> and CD8<sup>+</sup> T-cells (Fig. 9M), were alleviated in *Sting*<sup>gt/gt</sup> mice. All these indicate that GSDME-mediated pyroptosis contributes to aPD-1 therapy-associated myocarditis in a cGAS-STING-dependent manner.

### Pharmacological blockade of GSDME alleviates aPD-1 therapy-associated myocarditis and improves long-term survival in mice

Giving that GSDME-mediated pyroptosis boosts aPD-1 therapy-associated cardiotoxicity, targeting GSDME may be a potential therapeutic avenue for treatment of ICI-associated myocarditis. Thus, we tested the effects of blockade of GSDME in mice with aPD-1 therapy. Dimethyl fumarate (DMF), a pharmacological antagonist of GSDME via inhibiting

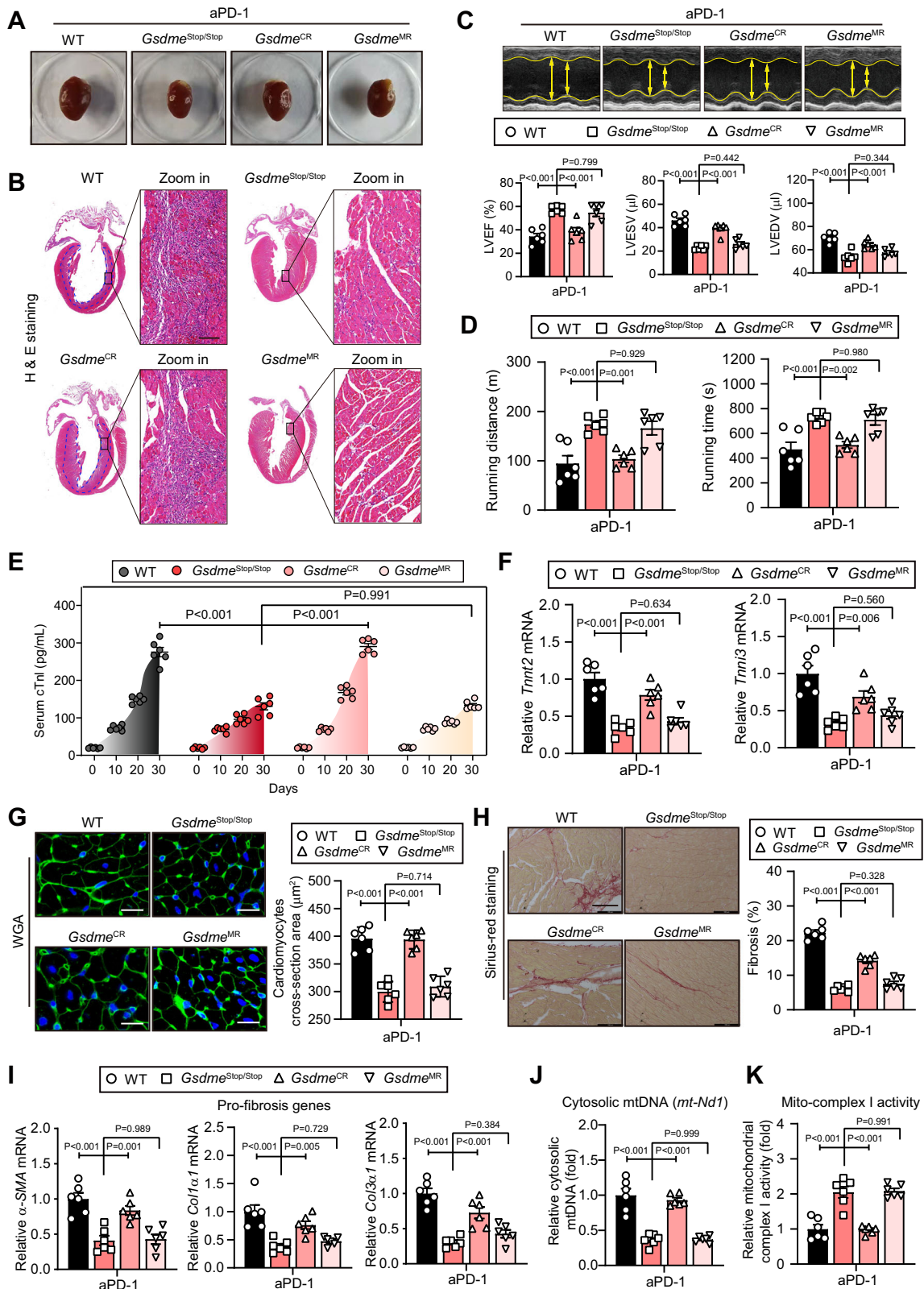
its interaction with caspases and subsequent processing and activation<sup>39</sup>, was used to block GSDME activation. Sequential administration of DMF followed by aPD-1 treatment successfully blocked the cleavage of GSDME in heart of mice upon aPD-1 treatment (Fig. 10A). In mice, DMF treatment not only attenuated aPD-1 therapy-induced cardiac hypertrophy (Fig. 10B), but also improved running distance and time in exercise exhaustion test (Fig. 10C). Echocardiography demonstrated that DMF rescued the cardiac dysfunction (Fig. 10D). The aPD-1 therapy-induced myocardial expressions of IFN-γ and STING were also significantly blunted by DMF (Fig. 10E).

We further tested the long-term outcome in another cohort of mice without tumour-bearing to exclude the interference of tumour-induced mouse death. Three groups of mice (*n* = 12 per group) were treated by IgG, aPD-1, and aPD-1 + DMF for 4 weeks respectively, and the cardiac malfunction in aPD-1-treated mice was confirmed by echocardiogram. Then, these mice were continuously monitored for more than 14 months. We observed that half of aPD-1-treated mice without tumor-bearing died within 12 months post aPD-1-treatment (Fig. 10F). H & E staining and TdT-mediated dUTP Nick-End Labeling (TUNEL) assay in the dying mice heart showed that there were massive infiltration of immune cells and dead cell in myocardium (Fig. 10G, H). Compared with aPD-1-treated mice, the mice in aPD-1 + DMF group had a significantly improved survival rate (Fig. 10F). Treatment of DMF alone did not cause any toxicity in normal mice and failed to inhibit tumor growth in mice (Supplementary Fig. 15). Taken together, these results indicate that pharmacological blockade of GSDME alleviates aPD-1 therapy-associated myocarditis.

## Discussion

There is mounting evidence suggesting that ICI leads to a significant infiltration of autoimmune cells into heart tissue in the early stage of ICI-associated myocarditis<sup>7,8,29,30,40</sup>. However, the subsequent immune activation and inflammatory responses following the infiltration of autoimmune cells, as well as the progression of inflammation in myocardium, remain poorly understood. Our findings may establish a molecular connection between pyroptosis and ICI-associated myocarditis by revealing the significant role of GSDME in this fatal irAEs (Fig. 10I).

In our study, we employed two mouse models with ICI-associated myocarditis. One model was induced by injecting antibodies against PD-1 into tumor-bearing mice, while the other was induced by injecting antibodies against CTLA4 into PD-1 knockout mice. The former model was designed to replicate the treatment of new-onset malignant patients typically with only anti-PD-1 antibody. Notably, approximately 70% of total cardiac irAEs are associated with the administration of anti-PD-1 antibody alone<sup>21</sup>. The latter model was utilized to simulate the treatment of advanced cancer patients undergoing combined therapy with both anti-PD-1 antibody and anti-CTLA4 antibody for improved survival<sup>33,34</sup>. As a result, our experimental setup encompassed both clinical scenarios. Remarkably, consistent results were observed in both models of ICI-induced myocarditis: the deletion of GSDME inhibited the development of ICI-induced myocarditis. Regarding the model induced by injecting antibodies against PD-1 into tumor-bearing



mice, it should be noted that anti-PD-1 treatment alone in normal C57BL/6 mice is not sufficient to induce myocarditis<sup>7-9</sup>, although deletion of PD-1 triggered immune cells accumulation in heart of C57BL/6 mice<sup>41</sup> and fatal autoimmune dilated cardiomyopathy in BALB/c mice<sup>27</sup>. By contrast, treatment of anti-PD-1 antibody alone is found to induce myocarditis in mice with an abnormal immune system. For instance, administration of PD-1 antibody produced

myocarditis in a melanoma C57BL/6 mice model<sup>30</sup> and tumor-free A/J mice<sup>9</sup>. Normal dose of anti-PD-1 antibody (100 - 200  $\mu$ g/dose, 3 - 4 doses in two weeks) for tumour elimination could induce ICI-associated cardiac dysfunction in several recent investigations<sup>30,42-44</sup>. However, it should be kept in mind that ICI-associated myocarditis was clinically observed a relatively low frequency (1-2%) in patients with normal dose of aPD-1 treatment. Thus, we used overdose of aPD-1



**Fig. 7 | Rescue of GSDME in cardiomyocyte but not in myeloid cell replicates aPD-1 therapy-induced cardiac dysfunction.** **A** Morphology of hearts isolated from tumour-bearing WT, *Gsdme*<sup>Stop/Stop</sup>, *Gsdme*<sup>CR</sup> and *Gsdme*<sup>MR</sup> mice received aPD-1 therapy. **B** Representative hematoxylin & eosin (H&E) staining and amplified images in whole heart section of WT, *Gsdme*<sup>Stop/Stop</sup>, *Gsdme*<sup>CR</sup> and *Gsdme*<sup>MR</sup> mice received aPD-1 therapy. The infiltrated immune cells were obviously noted in the myocardium of WT and *Gsdme*<sup>CR</sup> mice (blue dotted-line area) but not in *Gsdme*<sup>Stop/Stop</sup> and *Gsdme*<sup>MR</sup> mice. Scale bar, 200  $\mu$ m. **C** Representative echocardiograms and quantitative analyses of heart systolic functions, including left ventricular ejection fraction (LVEF), LV end systolic volume (LVESV) and LV end diastolic volume (LVEDV) in WT, *Gsdme*<sup>Stop/Stop</sup>, *Gsdme*<sup>CR</sup> and *Gsdme*<sup>MR</sup> mice received aPD-1 therapy. **D** Running distance and time of WT, *Gsdme*<sup>Stop/Stop</sup>, *Gsdme*<sup>CR</sup> and *Gsdme*<sup>MR</sup> mice received aPD-1 therapy in treadmill test. **E** Serum cTnI concentrations of WT, *Gsdme*<sup>Stop/Stop</sup>, *Gsdme*<sup>CR</sup> and *Gsdme*<sup>MR</sup> mice received aPD-1 therapy at different time-

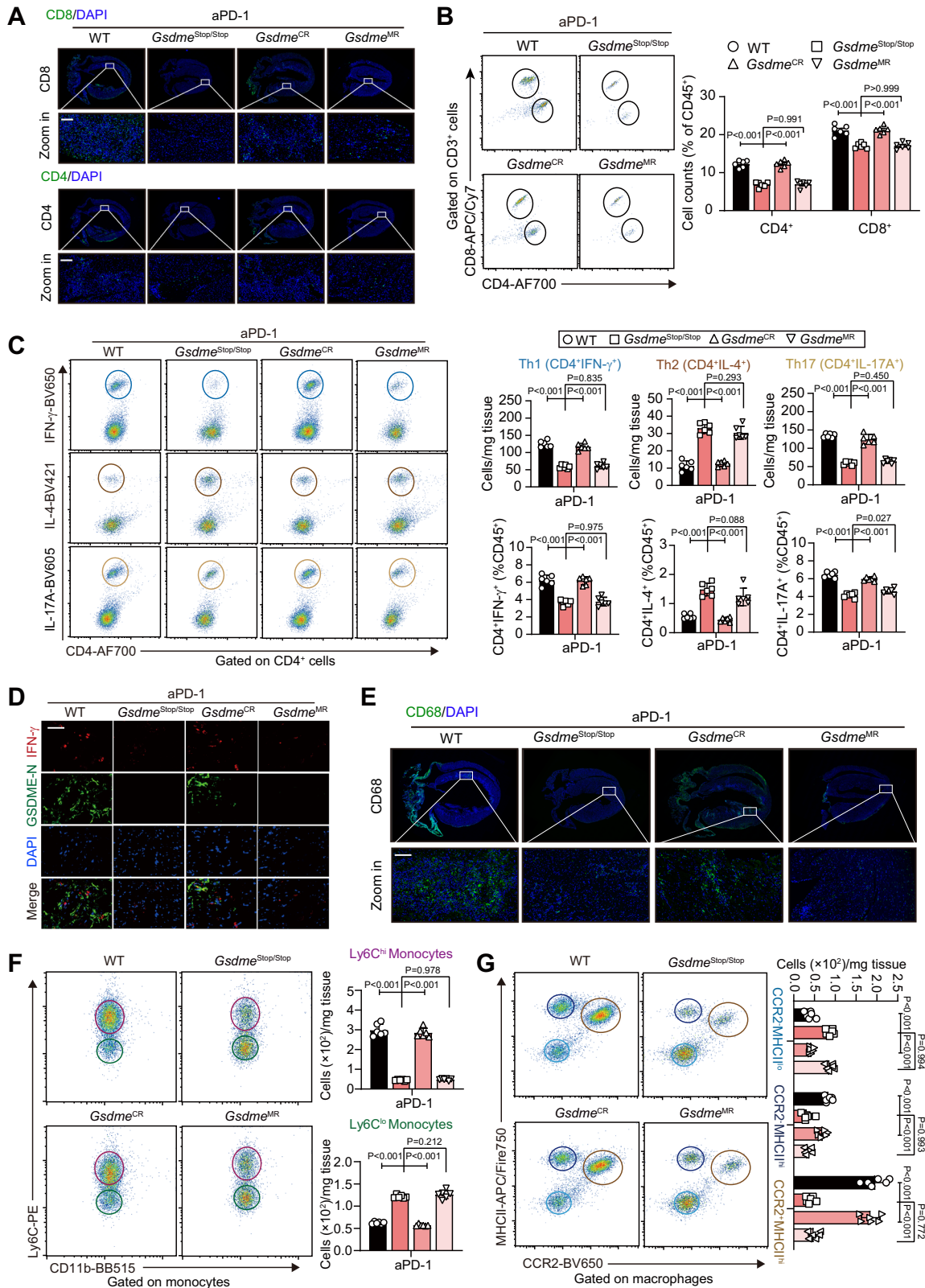
points. **F** Gene expression of *Tnnt2* and *Tnni3* in hearts of WT, *Gsdme*<sup>Stop/Stop</sup>, *Gsdme*<sup>CR</sup> and *Gsdme*<sup>MR</sup> mice received aPD-1 therapy. **G** Representative WGA staining in heart of WT, *Gsdme*<sup>Stop/Stop</sup>, *Gsdme*<sup>CR</sup> and *Gsdme*<sup>MR</sup> mice received aPD-1 therapy. Quantitative analysis of cardiomyocytes size was performed. Scale bar, 10  $\mu$ m. **H** Representative Sirius-Red staining in heart of WT, *Gsdme*<sup>Stop/Stop</sup>, *Gsdme*<sup>CR</sup> and *Gsdme*<sup>MR</sup> mice received aPD-1 therapy. Quantitative analysis of cardiac fibrosis was performed. Scale bar, 100  $\mu$ m. **I** Gene expression of pro-fibrosis factors ( *$\alpha$ -SMA*, *Colla1* and *Col3a1*) in heart of WT, *Gsdme*<sup>Stop/Stop</sup>, *Gsdme*<sup>CR</sup> and *Gsdme*<sup>MR</sup> mice received aPD-1 therapy. **J** Cytosolic mtDNA levels in heart tissue of WT, *Gsdme*<sup>Stop/Stop</sup>, *Gsdme*<sup>CR</sup> and *Gsdme*<sup>MR</sup> mice received aPD-1 therapy. **K** Myocardial mitochondrial complex I activities in WT, *Gsdme*<sup>Stop/Stop</sup>, *Gsdme*<sup>CR</sup> and *Gsdme*<sup>MR</sup> mice received aPD-1 therapy. The data were presented as means  $\pm$  SEM and analyzed by One-Way ANOVA followed by Tukey post-hoc test.  $n = 6$  biologically independent experiments.

antibody at 400  $\mu$ g/dose for four-weeks administration, and found this treatment successfully induced apparent myocarditis in almost all experimental mice. Recent investigations have revealed that the deletion of PD-1 alone was ineffective, whereas simultaneous deletion of PD-1 and CTLA-4 was necessary to induce fatal myocarditis in normal C57BL/6 mice<sup>8,31</sup>. To validate our findings from tumor-bearing mice treated with aPD-1 alone, we conducted additional experiments using a second type of ICI-induced myocarditis mouse model involving the combined inhibition of PD-1 and CTLA-4. Our observations indicated that anti-Ctla4-treated *Pdcd1*<sup>-/-</sup> *Gsdme*<sup>-/-</sup> mice were protected from ICI-induced myocarditis, as observed in anti-Ctla4-treated *Pdcd1*<sup>-/-</sup> mice. These results in the second model align with those obtained in the first model, reinforcing the crucial role of GSDME-mediated pyroptosis in ICI-associated myocarditis. In the anti-Ctla4-treated *Pdcd1*<sup>-/-</sup> mice, we observed slight increases in immune cells and pro-inflammatory factors mRNA expression in the diaphragm, suggesting a possible mild myositis in this region. In contrast, such mild changes were absent in skeletal muscles (quadriceps femoris muscle) and other organs. These phenotypes align with the observed respiratory muscle failure induced by ICI<sup>45</sup>. We acknowledge that in the first model of ICI-induced myocarditis with aPD-1 alone in tumor-bearing mice, the dose and frequency might have been higher than previously reported in tumor research, raising the possibility of cytokine release syndrome (CRS)<sup>46</sup>. However, as we did not observe any significant elevation of pro-inflammatory factors in the circulating PBMCs or systemic immune activation, the involvement of CRS in our setting can be ruled out.

The most important finding in the present study is that we identified GSDME-mediated pyroptosis as a key driver of ICI-induced myocarditis. Pyroptosis is considered to be a new type of RCD<sup>12</sup>. Previously, NOD-like receptor thermal protein domain associated protein 3 (NLRP3) and NLRP3-mediated inflammasome were considered as the major drivers of pyroptosis. With the discoveries of GSDMs family proteins<sup>14–16,47–49</sup>, GSDMs were proven to be the real executors of cell membrane disintegration in pyroptosis. GSDMD, a substrate of caspase-1 and caspase-4/5/11, is the earliest identified executor of pyroptosis<sup>14,15</sup>, while caspase-3-cleaved GSDME seems to a link between inflammatory-silent apoptosis and pyroptosis<sup>16,49–51</sup>. It is notable that not all cardiomyocytes were positive for GSDME-N in our model, suggesting that not all cardiomyocytes undergo cardiac pyroptosis. There are two possible causes for this observation. Firstly, the cardiomyocytes in close proximity to infiltrated immune cells may be particularly susceptible to harmful factors released by neighboring immune cells. In our model, we observed a preference for infiltrated immune cells to localize near the ventricular inner wall. The cardiomyocytes in these areas may start pyroptosis before other cardiomyocytes. Secondly, there may exist heterogeneity among cardiomyocytes when they encounter excessive stress in the context of myocarditis. In contrast to GSDMD, GSDME is silenced in most tumor cells but mainly expressed in normal tissues<sup>16</sup>. Aside from that, the difference between GSDMD-induced canonical pyroptosis and

GSDME-induced non-canonical pyroptosis is poorly understood. Our analyses with public scRNA-seq dataset clearly showed that *Gsdme*, but not *Gsdmd*, is abundantly expressed in cardiomyocytes, which do not support a key role of *Gsdmd* in heart due to its low expression in heart. Our results in mice model with conditionally rescue of *Gsdme* showed that GSDME, but not the canonical GSDMD, is the key cause of aPD-1-induced pyroptosis and myocarditis. These findings strongly support the notion that GSDME may be more important in normal tissue. We noted that it has been recently shown that caspase-11-dependent GSDMD cleavage mediated the ischemic injury-induced by acute myocardial infarction<sup>52,53</sup>. We speculated there might be different mechanisms between myocardial inflammation-induced by ICI and acute myocardial infarction since acute ischemic injury always involves dramatic hypoxic stress and irreversible sudden cell death. Additionally, it cannot be ruled out that cardiomyocytes could select other types of RCD in response to ICI stimuli in the blockade of GSDME-mediated pyroptosis because there was clear activation/upregulation of apoptotic caspases (caspase-3, 8 and 9) in the myocardium. Previously known as *DFNAs*, *GSDME* gene has numerous mutations in human<sup>34–38</sup>, which could cause hearing loss and other heritable disease. Since the gain-of-function and loss-of-function mutations of GSDME remarkably affect its expression and function, the mutations in *GSDME* gene could affect the cardiomyocytes fate and potentially contribute to the susceptibility of certain patients to ICI treatment. For example, gain-of-function mutation of GSDME may promote the switch of cell death in myocardium from “immune silent” apoptosis<sup>59</sup> towards inflamed pyroptosis. In this condition, myocarditis could be triggered and develops rapidly. By contrast, loss-of-function mutation of GSDME may inhibit the pyroptosis in myocardium. Nevertheless, this assumption needs further investigation.

The molecular events by which GSDME-mediated pyroptosis induces cell damage are not fully known. GSDME not only promotes pore formation in plasma membrane<sup>60</sup>, but also pores at mitochondrial membrane to augment inflammasome activation<sup>23</sup>. Using a proteomic analysis, we found that deletion of GSDME nearly depressed every aspect of immune function in heart, including mitochondrial DNA leakage, interferon response, antigen processing/presentation, neutrophil degranulation, etc. The observed mitochondrial leakage by pyroptotic injury may be a critical step in these pathological changes. Accordingly, the mice with aPD-1 therapy had increased cytosol mtDNA levels in heart and plasma. These prompted us to consider a role of cGAS-STING signalling, a central pathway that senses pathogenic exogenous and endogenous DNA to trigger innate immune reaction involving a strong IFN response<sup>61</sup>. In our setting, aPD-1 treatment induced activation of cGAS-STING pathway in WT mice but not in *Gsdme*<sup>-/-</sup> mice, implying that GSDME-mediated pyroptosis regulates cGAS-STING activation. Moreover, STING deficiency was also sufficient to block aPD-1 treatment-induced cardiac injury, GSDME cleavage and T-cell infiltration, suggesting there might be an IFN-dependent positive feedback loop (vicious cycle) which causes severe myocardial damage.



Currently, both GSDME<sup>17,18,62</sup> and STING<sup>63–66</sup> are hot topics in cancer immunotherapy. As GSDME gene is abundantly expressed in normal tissues<sup>16</sup> but kept at silent status epigenetically in tumour cells due to hypermethylation state on GSDME gene promoter region<sup>67</sup>, how to inhibit GSDME-mediated pyroptosis in normal tissues is worthy of attention. Considering that medicinal chemists have devoted great enthusiasm and efforts into designing and developing potent agonists

of STING pathway<sup>63–66</sup> for cancer immunotherapy, our results suggest that avoiding the GSDME-promoted pyroptosis and cGAS-STING-IFN signaling activation in heart during cancer immunotherapy, should be taken into account.

In summary, our findings revealed an activation of GSDME-mediated pyroptosis in PD-1 blockade-induced myocarditis in murine model and clinical patients. Additionally, we demonstrated that the

**Fig. 8 | Rescue of GSDME in cardiomyocytes but not in myeloid cells replicates aPD-1 therapy-induced cardiac immune cells infiltration and inflammation.**

**A** Representative fluorescent immunohistochemistry staining of CD8 and CD4 and amplified images in whole heart section of WT, *Gsdme*<sup>stop/stop</sup>, *Gsdme*<sup>CR</sup> and *Gsdme*<sup>MR</sup> mice received aPD-1 therapy. The infiltrated CD8<sup>+</sup> and CD4<sup>+</sup> T-cells were obviously noted in the myocardium of WT and *Gsdme*<sup>CR</sup> mice, which were partially inhibited in *Gsdme*<sup>stop/stop</sup> and *Gsdme*<sup>MR</sup> mice. Scale bar, 100  $\mu$ m. **B** Representative flow cytometry and quantitative analysis of CD4<sup>+</sup> and CD8<sup>+</sup> cells in heart of WT, *Gsdme*<sup>stop/stop</sup>, *Gsdme*<sup>CR</sup> and *Gsdme*<sup>MR</sup> mice received aPD-1 therapy. **C** Proportions of Th1 (IFN- $\gamma$ <sup>+</sup>), Th2 (IL-4<sup>+</sup>) and Th17 (IL-17A<sup>+</sup>) cells within CD4<sup>+</sup> T-cells in hearts of WT, *Gsdme*<sup>stop/stop</sup>, *Gsdme*<sup>CR</sup> and *Gsdme*<sup>MR</sup> mice received aPD-1 therapy. **D** Double-fluorescent immunohistochemistry of IFN- $\gamma$  and GSDME-N in heart of WT, *Gsdme*<sup>stop/stop</sup>, *Gsdme*<sup>CR</sup> and *Gsdme*<sup>MR</sup> mice received aPD-1 therapy. DAPI was used to stain nuclei. Scale bar,

50  $\mu$ m. **E** Representative fluorescent immunohistochemistry staining of CD68 and amplified images in whole heart section of WT, *Gsdme*<sup>stop/stop</sup>, *Gsdme*<sup>CR</sup> and *Gsdme*<sup>MR</sup> mice received aPD-1 therapy. The infiltrated CD68<sup>+</sup> MOs/MPs were obviously noted in the myocardium of WT and *Gsdme*<sup>CR</sup> mice, which were partially inhibited in *Gsdme*<sup>stop/stop</sup> and *Gsdme*<sup>MR</sup> mice. Scale bar, 100  $\mu$ m. **F** Representative flow cytometry plots and quantitative analysis of Ly6C<sup>hi</sup>CD11b<sup>+</sup> and Ly6C<sup>lo</sup>CD11b<sup>+</sup> monocytes in heart of WT, *Gsdme*<sup>stop/stop</sup>, *Gsdme*<sup>CR</sup> and *Gsdme*<sup>MR</sup> mice received aPD-1 therapy. **G** Representative flow cytometry plots and quantitative analysis of CCR2<sup>+</sup>MHC-II<sup>lo</sup>, CCR2<sup>+</sup>MHC-II<sup>hi</sup> and CCR2<sup>-</sup>MHC-II<sup>hi</sup> macrophages in heart of WT, *Gsdme*<sup>stop/stop</sup>, *Gsdme*<sup>CR</sup> and *Gsdme*<sup>MR</sup> mice received aPD-1 therapy. The data were presented as means  $\pm$  SEM and analyzed by One-Way ANOVA followed by Tukey post-hoc test.  $n = 6$  biologically independent experiments.

GSDME in cardiomyocytes, but not myeloid cells, triggers myocarditis via a mtDNA-cGAS-STING-dependent manner. Thus, targeted inhibition of GSDME-cGAS-STING axis may be a potential strategy for prevention or management of ICI-associated myocarditis and other irAEs.

**Methods****Mice**

C57BL/6J mice were purchased from Shanghai SLAC Laboratory Animal Co., Ltd. (Shanghai, China). The *Lysm*-Cre mice (B6.129P2-*Lyz2*<sup>tm1.1cre</sup>/J, #004781), *Myh6*-Cre mice (B6.FVB-Tg(*Myh6-cre*)2182Mds/J, #011038) and STING-goldenticket (*Sting*<sup>gsl/gsl</sup>) mice (C57BL/6J-*Sting*<sup>gsl</sup>/J, #017537) were obtained from The Jackson Laboratory. Global GSDME knockout mice (*Gsdme*<sup>-/-</sup>) were generated by Shanghai Model Organisms Center, Inc (China, Shanghai). The *Pdcd1*<sup>-/-</sup> mice (C57BL/6N-*Pdcd1*<sup>em1C</sup>/Cya, #S-KO-03581) and *Gsdme*<sup>stop/stop</sup> mice were generated by Cyagen Biosciences Inc (Guangzhou, China). *Gsdme*<sup>-/-</sup> mice were crossed with *Pdcd1*<sup>-/-</sup> mice to produce *Gsdme*<sup>-/-</sup>*Pdcd1*<sup>-/-</sup> mice. The *Gsdme*<sup>stop/stop</sup> mice were crossed with *Myh6*-Cre mice or *Lysm*-Cre to produce *Gsdme*<sup>stop/stop</sup>;*Myh6*-Cre and *Gsdme*<sup>stop/stop</sup>;*Lysm*-Cre mice. All mice were viable, fertile and normal in size without any gross physical or behavioral abnormalities. For all experiments, mice were allocated into experimental or control groups randomly. Mice were maintained on a 12-hour light/dark cycle in a specific pathogen-free facility in a temperature-controlled (23  $\pm$  2  $^{\circ}$ C) and humidity-controlled (40  $\pm$  5%) environment. Chow and water were freely available. The use of animals, including all treatments, was approved by the Institutional Animal Care and Use Committee of Shanghai Tenth People's Hospital of Tongji University and compliant with the Guide for the Care and Use of Laboratory Animals published by the US National Institutes of Health (NIH Publication 8th edition, update 2011).

**Mouse models of ICI-induced myocarditis**

Two animal models were used in the present studies. The first model was achieved using aPD-1-treatment in tumor-bearing mice. The 8–12-week-old WT or *Gsdme*<sup>-/-</sup> mice were subcutaneously transplanted in the flank with  $2 \times 10^5$  MC38 mouse colon adenocarcinoma cells (Cell Center of Chinese Academy of Medical Sciences) in 200  $\mu$ l Matrigel/PBS (1:1, BD Biosciences) to induce tumour development. The tumor was allowed to growth for 7 days. The mice without tumor were excluded. Three days later, the mice were intraperitoneally injected with monoclonal anti-mouse PD-1 antibody (400  $\mu$ g/dose, qod, BioXcell, clone 29 F.1A12, #BE0273) or normal IgG (clone: 2A3, BioXcell) for 4 weeks. For DMF treatment, DMF was injected intraperitoneally (50 mg/kg, qod) at 1 h post aPD-1 injection. The second model with ICI-induced myocarditis was achieved using anti-Ctla4 treatment in *Pdcd1*<sup>-/-</sup> or *Gsdme*<sup>-/-</sup>*Pdcd1*<sup>-/-</sup> mice. The monoclonal anti-mouse Ctla4 antibody (BioXcell, IgG2b, clone: 9D9, #BE0164) at a normal dose (200  $\mu$ g/dose, i.p., 4 injections in 20 days) was administered. In this study, only male mice were utilized to induce ICI-myocarditis, aiming to minimize variability factors, as females tend to display greater resistance to myocarditis compared to males<sup>68</sup>.

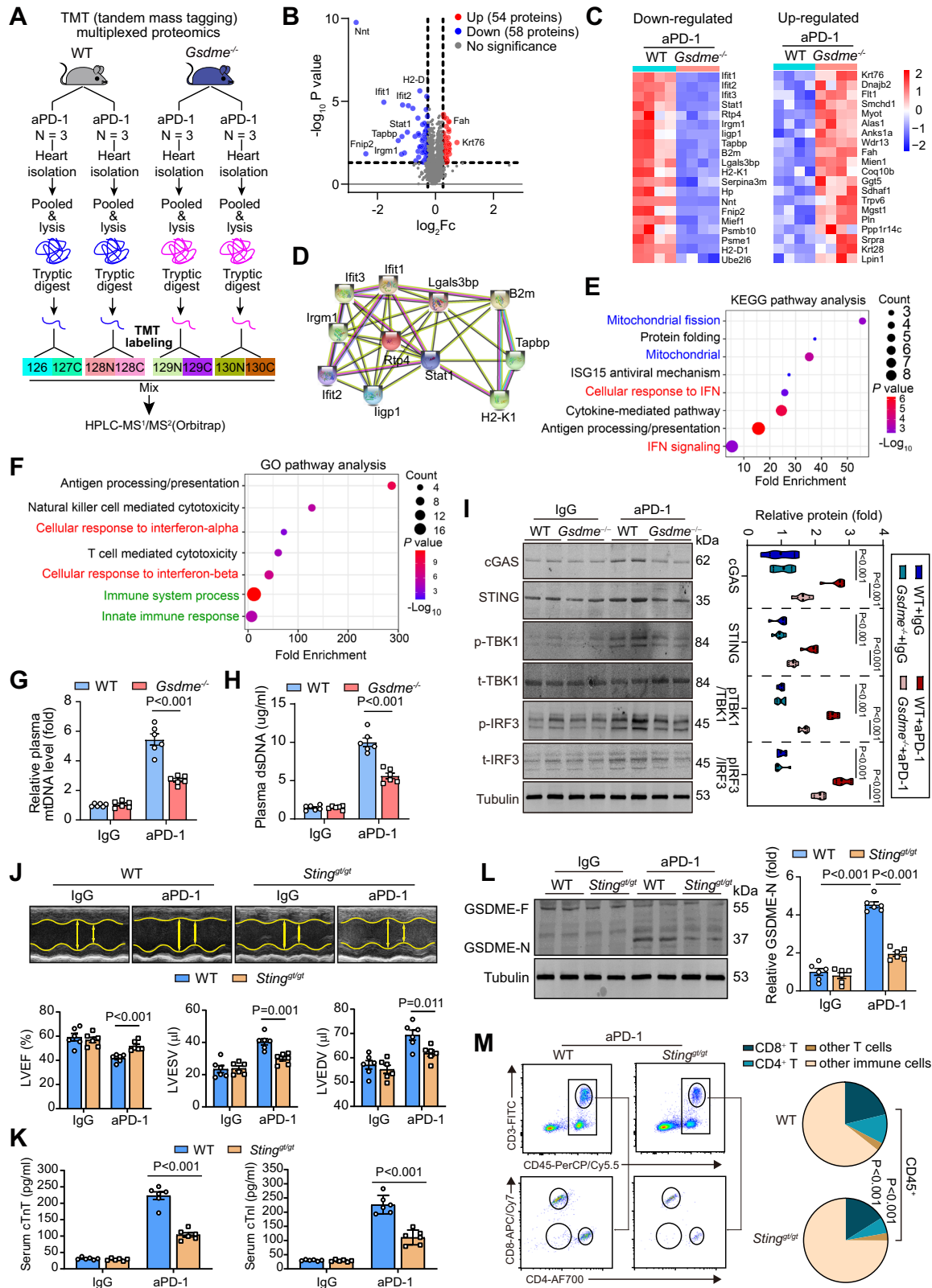
**Human study**

Human samples were taken from patients at Shanghai Changzheng Hospital and Shanghai Tenth People's Hospital between 2017 and 2022 as part of a trial published in recent works (No. NCT03239015)<sup>25,26</sup>. The original primary aim of the trial was to evaluate the efficacy of targeted preivision therapy in patients with refractory tumours, and any adverse drug reactions in cancer patients were monitored. The trial was authorized by the ethical review board and institutional approval from Shanghai Changzheng Hospital (No. 2017SL016). After the first course of therapy, the patients were screened according to International Society of Cardio-Oncology (IC-OS) 2021 Consensus<sup>24</sup>. The exclusion criteria include special situation that patients were: (1) severe organ failure due to tumor growth; (2) with heart diseases such as myocardial infarction and heart failure before aPD-1 treatment; (3) with radiotherapy or other chemotherapy. In this study, a total of 360 patients with tumor who underwent at least one course of aPD-1 therapy by anti-PD-1 antibody were monitored. After screening, a total of 6 patients diagnosed with myocarditis were included to this study for comparison of their blood GSDME concentrations at baseline and after aPD-1 therapy. Since the objective was specific (evaluating serum GSDME levels), this work is not part of the clinical trial. The characteristics of these 6 patients with myocarditis were illustrated in Supplementary Table 1. Additionally, a total of 30 age- and gender-matched tumor patients without any myocardial with myocarditis phenotypes were screened as control. This study was performed according to the declaration of Helsinki and approved by the Ethics Committee of Shanghai Changzheng Hospital (2017SL016) and Shanghai Tenth People's Hospital (2019-K-032). We have the consent of the Institutional review board (IRB) and the Data and Safety Monitoring Board (DSMB) of Shanghai Changzheng Hospital and Shanghai Tenth People's Hospital. We have consents to use human samples from these hospitals. All patients have given their informed consent for the storage and utilization of their data and biomaterials for research purposes.

**Echocardiography**

Transthoracic echocardiography was performed with Vevo 2100 high-frequency ultrasound system (VisualSonic, Toronto, ON, Canada) equipped with an MS-550S imaging transducer (22–55 MHz). Mice were anesthetized by 5% isoflurane and maintained in the supine position on a heated, bench-mounted adjustable rail system. Then isoflurane was reduced to 1–2% so that heart rate could be maintained at 450  $\pm$  50 bpm, while the heating pad was used so that body temperature could be controlled at 37.0  $^{\circ}$ C  $\pm$  0.5  $^{\circ}$ C. Systolic function was measured from short axis M-mode echocardiographic images at the midventricular level. Left ventricular ejection fraction (LVEF) and left ventricular fractional shortening (LVFS), left ventricular end systolic volume (LVESV) and left ventricular end diastolic volume (LVEDV) were calculated. All images were analyzed using dedicated software (Vevo 2100 v3.1.1, VisualSonics).





**Exercise exhaustion test**

An exercise exhaustion test was performed as described previously in ref. 69. Mice were acclimatized to treadmill exercise running (Columbus Instruments) for 2 days (uphill 20°, 10 m/min, 15 min). After adapted to treadmill exercise, mice were forced to run uphill (20°) at speeds of 5 m/min for 4 min and 15 m/min for 2 min. Every subsequent 2 min, the speed was increased by 2 m/min until mice were unable to

return to running within 10 s of direct contact with an electric-stimulus grid. Running time and distance of exhaustion were measured.

**Cell extraction**

Single cell suspensions were obtained from heart and spleen as described previously<sup>70,71</sup>. For cell extracting from heart, the mice were anesthetized and the hearts were harvested. After removing the aorta

**Fig. 9 | cGAS-STING signalling mediates aPD-1 therapy-induced myocarditis.**

**A** A schematic graph showing the procedure of isobaric Tandem Mass Tagging (TMT)-based multiplexed quantitative proteomic analysis in heart of WT and *Gsdme*<sup>-/-</sup> mice received aPD-1 therapy. **B** Volcano plot showing the upregulated and downregulated proteins identified by TMT quantitative proteomic analysis. **C** Heatmaps showing the top 20 up-regulated and down-regulated proteins in *Gsdme*<sup>-/-</sup> mice heart compared with WT mice heart upon aPD-1 therapy. **D** The potential protein-protein interaction among the top differentially regulated proteins between WT and *Gsdme*<sup>-/-</sup> mice heart upon aPD-1 therapy. The protein-protein interaction network analysis was performed with STRING database v 11.0. **E** Top enriched pathways in Kyoto Encyclopedia of Genes and Genomes (KEGG) database with the most differentially regulated proteins between WT and *Gsdme*<sup>-/-</sup> mice heart upon aPD-1 therapy. **F** Top enriched pathways in Gene Ontology (GO) knowledgebase with the most differentially regulated proteins between WT and

*Gsdme*<sup>-/-</sup> mice heart upon aPD-1 therapy. **G, H** The plasma levels of mtDNA and double stranded DNA (dsDNA) in WT and *Gsdme*<sup>-/-</sup> mice heart upon aPD-1 therapy. **I** Expression of cGAS, STING, phospho-TBK1 (p-TBK1), total-TBK1, phospho-IRF3 (p-IRF3) and total-IRF3 in heart of WT and *Gsdme*<sup>-/-</sup> mice received aPD-1 therapy or control IgG were determined using immunoblotting. **J** Representative echocardiograms and quantitative analysis of cardiac function in WT and *Sting*<sup>gt/gt</sup> mice received aPD-1 therapy. **K** Serum cTnT and cTnI concentrations of WT and *Sting*<sup>gt/gt</sup> mice received aPD-1 therapy or control IgG. **L** Cleavage of GSDME in WT and *Sting*<sup>gt/gt</sup> mice received aPD-1 therapy or control IgG. **M** Representative flow cytometry showing the proportions of CD4<sup>+</sup> and CD8<sup>+</sup> cells in heart of WT and *Sting*<sup>gt/gt</sup> mice received aPD-1 therapy. The data were presented as means ± SEM and analyzed by two-sided unpaired Student's t-tests. *n* = 6 biologically independent experiments.

and epicardium adipose, the heart was cut into small pieces (1 mm × 1 mm × 1 mm) and repeatedly washed in saline to remove blood cells. These cardiac pierces were digested in Hanks' Balanced Salt Solution (HBSS) with type II collagenase (0.08%, Worthington) and DNase I (10 mU/ml, Sigma) at 37 °C for 40 min. The cell-containing samples were passed with a cell strainer (70 μm) to remove undigested tissue pieces. To completely digest the heart tissue, the above steps were repeated 3 times. The cell viability was greater than 98% using the trypan blue exclusion. For cell extracting from spleen, the spleen was isolated, placed in HBSS and gently minced with a scalpel repeatedly. Single cells suspensions were obtained by passing small pieces of spleen through 70 μm cell strainers. The single cells suspensions were transferred to fresh tubes and centrifuged at 4 °C and 300 g for 10 min. The pellet was re-suspended in 0.4 ml of RBC lysis buffer (eBiosciences) for 5 min at room temperature. Splenocytes were collected after centrifugation (10 min, 300 g) and then re-suspended.

**Subcellular fractionation**

The single cells prepared as abovementioned were resuspended in 150 μl digitonin lysis buffer (150 mM NaCl, 50 mM HEPES pH7.4, 25 μg/ml Digitonin, Protease and phosphatase inhibitors) and incubated on a rotator for 20 min. The lysates were centrifuged at 2000 g for 10 min at 4 °C to collect supernatants, which were then harvested and centrifuged for 30 min at 20,000 g at 4 °C. The supernatant was transferred to a new tube and centrifuged for additional 30 min at 20000 g at 4 °C. This centrifugation was repeated for 4 times. The final supernatant is considered to be the cytosolic fraction. For mitochondria isolation, a commercial kit (Sigma-Aldrich, MITOISO1) was used. The tissues were lysed and the isolation process was performed according to the manufacturer's instruction.

**Multiplexed flow cytometry**

Single cell suspension of heart was prepared as described previously. Mice were euthanized, after which the hearts were perfused with cold perfusion buffer. After collecting the anterior wall of the left ventricle, the tissue was washed in ice-cold perfusion buffer, kept on ice, minced into small pieces, and transferred into a culture flask with cold digestion buffer as described above. After digestion of the tissue, the cell suspension was gently pipetted up and down, after which the lysate was passed through a 100 μm cell strainer. The strainer was then rinsed with DMEM, and the cells were collected. Isolated cell suspensions were incubated with fluorophore labeled antibodies for 30 min at room temperature away from light. The primary antibodies used for flow cytometry were listed in Supplementary Table 3. After incubation, the single cell suspensions were centrifuged at 4 °C and 300 g for 10 min. Pellets were washed and re-suspended using flow cytometry buffer and analyzed using a CytofLEX-S cytometer (Beckman). Data were analyzed with FlowJo software (version 10.0.0) with t-SNE-guided

gating strategy as described previously<sup>72</sup>. More information regarding the gating strategy were illustrated in Supplementary Table 5.

**RNA isolation and qPCR**

Total RNA of mice hearts was extracted with TRIzol reagent (Thermo Fisher Scientific) according to the manufacturer's recommendation. The quality of RNA was evaluated using Quawell Q5000 UV-spectrophotometer (Quawell, San Jose, CA). A total of 500 ng RNA was used for reverse transcription using TransScript<sup>®</sup> First-Strand cDNA Synthesis SuperMix (TransGen Biotech). Real-time quantitative PCR (qPCR) reactions were performed in triplicate with TB Green Premix Ex Taq Mixture II (Takara, Tokyo, Japan) using CFX96 Real Time PCR Detection System (BioRad). GAPDH was used for normalization. The 2<sup>-ΔΔCt</sup> relative quantification method was used to estimate the amount of target mRNA in samples. Primer sequences were listed in Supplementary Table 3.

**Cytosolic and plasma mtDNA quantification**

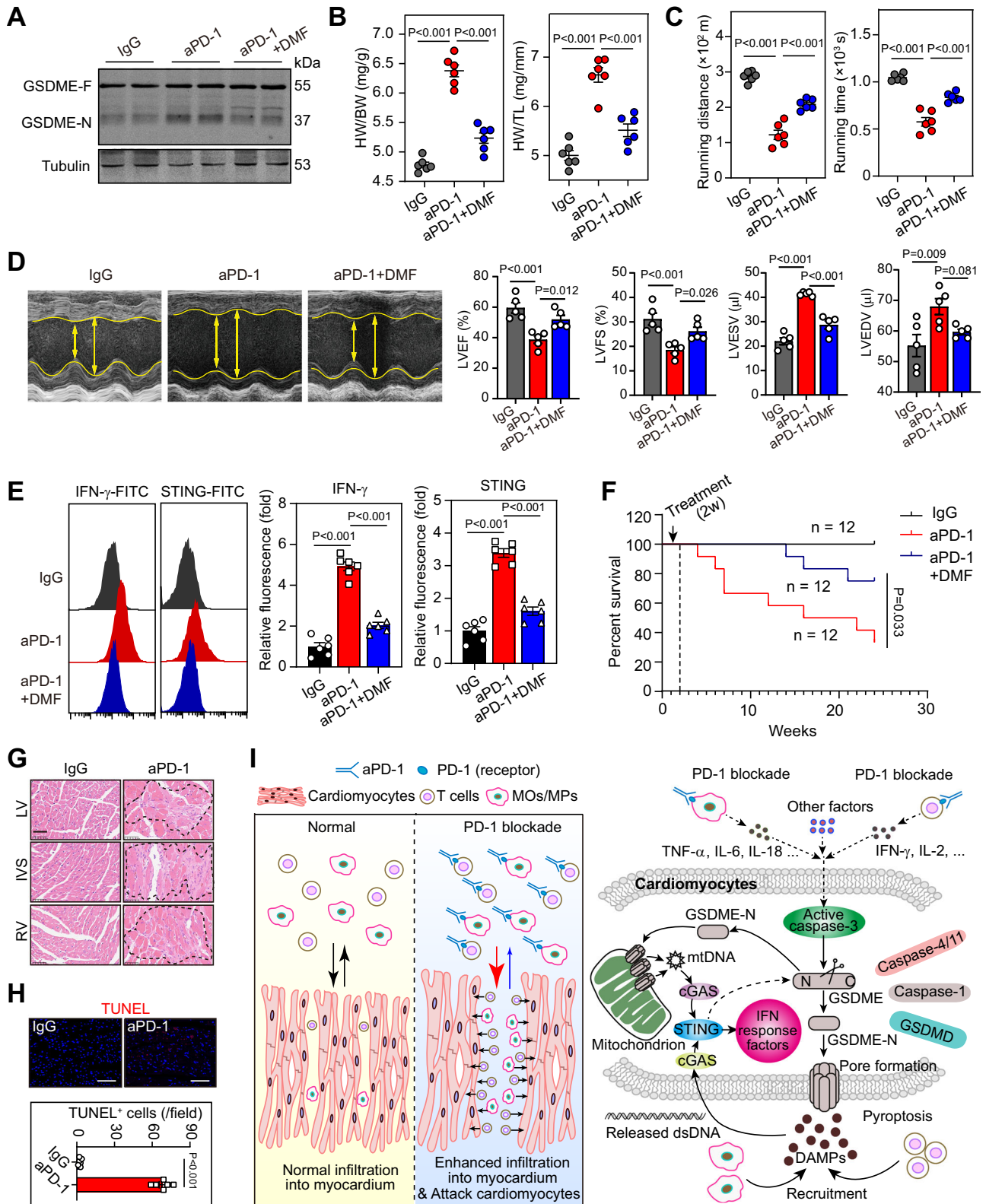
Cytosolic fraction was extracted from heart tissues and the DNA in cytosolic fraction was isolated using DNA extracting kit. For mtDNA quantification, two mitochondrial genes *mt-Nd1* and *D-loop* were measured by normalization to a nuclear 18 S RNA in nuclear extraction. The 2<sup>-ΔΔCt</sup> relative quantification method was used to estimate the amount of cytosolic mtDNA. For plasma mtDNA evaluation, the mtDNA was isolated from plasma using the Qjamp DNA Micro Kit (Qiagen, Valencia, CA) per vendor's directions. *mt-Nd1* was used to determine the plasma mtDNA levels. The linearity of the quantitative assay was assessed using the template cloned into plasmid DNA and serially diluted to prepare a series of calibrators with known concentrations. Absolute values of MtDNA copy number were determined by calculation from the standard curve. Primer sequences were listed in Supplementary Table 3.

**Immunoblotting**

Mouse tissue or cells were homogenized in ice-cold RIPA buffer containing protease and phosphatase inhibitors (Sigma). Lysates were cleared by centrifugation at 13,000 g for 15 min at 4 °C. The concentrations of protein lysates were determined by a Bradford assay. Proteins were separated by 8–15% SDS-PAGE gels and transferred to nitrocellulose membranes. Membranes were incubated for 1 h with 5% BSA-PBS and incubated with different primary antibodies at 4 °C overnight. Primary antibodies were listed in Supplementary Table 3. After washing, membranes were incubated with secondary antibodies conjugated with IRDye<sup>®</sup> 800CW (Li-Cor Biosciences)<sup>73</sup>. Images were photographed with Odyssey system (Li-Cor Biosciences) and then analyzed with Image J software.

**Histology**

Mouse hearts were fixed in 10% formalin overnight and paraffin-embedded. The paraffin-embedded hearts were cut to five-micron



sections. H & E staining and Sirius-red staining were performed on these sections according to the general protocols. The stained sections were scanned by 3DHISTECH Panoramic SCAN (Hungary) and analyzed with CaseViewer Software.

**Immunohistochemistry and immunofluorescence**

Isolated hearts were fixed in 4% PFA at 4 °C overnight and dehydrated in 30% sucrose. After embedded in OCT Compound, sections (10  $\mu$ m)

were blocked in 5% normal goat plasma for 1 h at room temperature. The sections were incubated with primary antibodies overnight at 4 °C. The primary antibodies were listed in Supplementary Table 3. On the next morning, the sections were washed in PBS solution for three times and incubated with secondary antibodies conjugated with Alexa Fluor-488 dye (Invitrogen), Alexa Fluor-555 dye (Invitrogen) or horseradish peroxidase (ProteinTech) for 1 h at room temperature. In immunohistochemistry analysis, sections were counterstained with



**Fig. 10 | Pharmacological blockade of GSDME alleviates myocarditis and improves long-term survival in aPD-1 therapy-treated mice.** **A** Cleavage of GSDME in heart of normal IgG, aPD-1-treated and aPD-1 + DMF-treated mice.  $n = 6$  biologically independent experiments. **B** HW/BW ratio and HW/TL ratio of normal IgG, aPD-1-treated and aPD-1 + DMF-treated mice.  $n = 6$  biologically independent experiments. **C** Running distance and time of normal IgG, aPD-1-treated and aPD-1 + DMF-treated mice in an exercise exhaustion test.  $n = 6$  biologically independent experiments. **D** Representative echocardiograms and quantitative analysis of cardiac function of normal IgG, aPD-1-treated and aPD-1 + DMF-treated mice.  $n = 5$  biologically independent experiments. **E** Representative flow cytometry showing the expression of IFN- $\gamma$  and STING in heart of normal IgG, aPD-1-treated and aPD-1 + DMF-treated mice.  $n = 6$  biologically independent experiments. **F** Monitoring of long-term survival in normal IgG, aPD-1-treated and aPD-1 + DMF-treated mice.  $n = 12$  per group. The cardiac dysfunction of these mice at 4 weeks post aPD-1 injection was confirmed using echocardiography. **G** Hematoxylin & eosin staining

was performed in heart of dying mice receiving aPD-1-treatment to confirm the immune cells infiltration of myocarditis.  $n = 6$  biologically independent experiments. Scale bar, 50  $\mu\text{m}$ . **H** TUNEL staining was performed in heart of dying mice receiving aPD-1-treatment to confirm the cell death in hearts of mice.  $n = 6$  biologically independent experiments. Scale bar, 50  $\mu\text{m}$ . **I** A working model for the role of GSDME-dependent pyroptosis in myocarditis induced by PD-1 blockade. Left: Blockade of PD-1 triggers infiltration of T-cells and myeloid cells into myocardium. The cardiomyocytes are attacked by the activated T-cells and myeloid cells, and become dysfunctional and hypertrophic. Right: The cGAS-STING-IFN signal is triggered by mtDNA and dsDNA released after GSDME-mediated pyroptosis-dependent cardiac damage, which further maintains and amplifies the myocardial inflammation. The data were presented as means  $\pm$  SEM and analyzed by Log-Rank test (**F**) and two-sided unpaired Student's *t*-test (**H**) and One-Way ANOVA followed by Tukey host test (other panels).

haematoxylin. In immunofluorescence analysis, nuclei were counterstained in DAPI (Invitrogen). For WGA staining, the sections were stained using Alexa Fluor 488-conjugated WGA (Invitrogen, 1:500) reagent in accordance with the manufacturer's instructions and then counterstained with DAPI. The stained sections were scanned by 3DHISTECH Panoramic SCAN (Hungary) and analyzed with CaseViewer Software. The cross-sectional area was analyzed using Image J software.

### TUNEL

The immunofluorescence TUNEL assay was performed with a commercial In situ Cell Death Detection Kit<sup>®</sup> according to the instructions of the manufacturer<sup>74</sup>. Images were obtained by confocal microscopy (Olympus, Fluoview FV1000, Tokyo, Japan).

### Biochemical assays

The serum concentrations of CK-MB, cTnT, cTnI, and NT-proBNP, as well as other parameters, were measured in an automatic biochemical analyzer (Beckman-Coulter, USA). The blood numbers of monocytes and lymphocytes in patients were also measured with the automatic biochemical analyzer. The concentrations IL-1 $\beta$ , IL-18 and IL-6 in the mice serum were determined with commercial ELISA kits (R & D systems) following the manufacturer's instructions. The serum concentrations of GSDME in patients were determined using an ELISA kit (#AG-45B-0024-KI01) from Adipogen Life Sciences (San Diego, CA). The mitochondrial complex I and IV activity were measured using ELISA kits from Abcam (#ab287847) and Solarbio (#BC0945) respectively. The NAD<sup>+</sup> in mitochondria fraction was evaluated using a commercial kit from Abcam (ab65348). The ATP and GSH levels in mitochondria fraction were measured using commercial kits from Solarbio (#BC0300 and #BC1175). The plasma dsDNA level was measured by Quant-iT PicoGreen dsDNA Reagent and kits (Thermo Fisher Scientific) according to the manufacturer's protocol.

### Transmission electron microscopy (TEM)

Heart tissue was fixed with 2% paraformaldehyde and 2% glutaraldehyde in 0.1 mol/L phosphate buffer (pH 7.4), followed by postfixation for 8 h in 1.5% osmium tetroxide. After dehydration with graded alcohols, the samples were dehydrated in a graded ethanol series and embedded in epoxy resin. Samples were sectioned (80 nm), counterstained with uranylacetate and lead citrate and observed with a transmission electron microscope (Hitachi, H-800, Tokyo, Japan)<sup>75</sup>. Images were acquired digitally from a randomly selected pool of 3 to 5 fields under each condition.

### Proteomics

Hearts were infused with PBS, frozen in liquid nitrogen and thoroughly ground to powder and then lysed in extraction buffer (8 M urea, 1% Triton X-100, 1% Protease inhibitor). Lysates was centrifuged at 12,000 g

at 4 °C for 10 min and the supernatant was transferred to a new centrifuge tube. The concentration of protein was determined using BCA kit. Dithiothreitol (DTT) was added to protein samples to make the final concentration of 5 mM at 56 °C for 30 min, and then alkylated with iodoacetamide (IAA) was added to make the final concentration of 11 mM for 15 min at room temperature away from light. Trypsin was added to completely digest the protein. Strata X C18 (Phenomenex) was used for de-salting the hydrolyzed peptides. After vacuum-dried and dissolved with 0.5 M TEAB, the peptides samples were then labelled using the TMT Plex Labelling Kit (Thermo Fisher Scientific, Rockford, IL). Labeled peptides were subjected to peptide separation into different fractions using reversed phase high performance liquid chromatography. The fractionated peptides were then analyzed by Ultra performance liquid chromatography-tandem mass spectrometry (EASY-nLC-MS/MS). Peptide precursor ions and their secondary fragments are detected and analyzed using a full-scan high-resolution Orbitrap mass spectrometry (Thermo Fisher Scientific). Maxquant (v1.5.2.8) was used to identify protein. According to Fold change > 1.2 and  $P < 0.05$ , the differentially expressed proteins were selected. The differentially expressed proteins between WT and *Gsdme*<sup>-/-</sup> mice upon aPD-1 therapy were subjected with Gene Ontology (GO) and Kyoto Encyclopedia of Genes and Genomes (KEGG) bioinformatic analyses using DAVID Bioinformatics Resources 6.8 (<https://david.ncifcrf.gov>). The protein-protein interaction network analysis was performed with STRING database v 11.0. The raw MS data for proteomics were deposited in iProx database with identifier IPX0004084000.

### scRNA-seq data analysis

Datasets of scRNA-seq were obtained from the NCBI Gene Expression Omnibus (GEO) database with identifiers GSE162959, GSE232466, and GSE180045. R 4.2.3 (R Core Team, Vienna, Austria) and RStudio software were used to analyze and process the scRNA-seq data. The quality of cells was assessed based on the following metrics: 1) Cells that simultaneously expressed gene expression patterns of two cell types were removed. 2) Genes that were not detected in  $\geq 3$  cells were removed. 3) Cells with <200 unique transcripts detected were removed. 4) Cells with > 15% mitochondrial read counts were removed. After log normalization and TPM-like (base 10,000) normalization, the data were analyzed using the Seurat package (version 4.0.3, accessible at <https://satijalab.org/seurat>). This resulted in scaled data, upon which a PCA was conducted using the top 2000 most variable genes. Subsequently, the leading 15 principal components were selected to build a UMAP with a resolution parameter of 0.8. Through a graph-based clustering approach, we achieved unsupervised clustering of cells based on these top 15 PCA components. To identify marker genes, we utilized the FindAllMarkers function, incorporating the Wilcox rank sum test, under specified criteria: a log<sub>2</sub> fold change greater than 0.25, a *p*-value less than 0.05, and a minimum percentage of cells expressing the gene exceeding 0.1.

### Statistical analysis

For echocardiography, flow cytometry and immunohistochemistry/immunofluorescence, blinding was performed. Data are represented as mean values  $\pm$  standard error of the mean (SEM). Information about statistical details and methods is included in the figure legends. Statistical analysis was performed with the two-tailed unpaired Student's *t* test, paired Student's *t* test, or One-Way ANOVA followed by Tukey's post test. Survival curves were analyzed using log-rank analysis. GraphPad Prism 8 (GraphPad Software, California, USA) was used to perform statistics.  $P < 0.05$  was considered statistically significant.

### Reporting summary

Further information on research design is available in the Nature Portfolio Reporting Summary linked to this article.

### Data availability

Data supporting the findings described in this manuscript are available in the article, Supplementary Information, Source data file and from the corresponding author upon request. Proteomics data is deposited in iProX database with identifier [IPX0004084000](https://www.iprox.org/). The public datasets of GSE162959, GSE232466 and GSE162959 were downloaded from GEO database. Source data are provided with this paper.

### References

- Martins, F. et al. Adverse effects of immune-checkpoint inhibitors: epidemiology, management and surveillance. *Nat. Rev. Clin. Oncol.* **16**, 563–580 (2019).
- Johnson, D. B. et al. Fulminant Myocarditis with Combination Immune Checkpoint Blockade. *N. Engl. J. Med.* **375**, 1749–1755 (2016).
- Thuny, F., Naidoo, J. & Neilan, T. G. Cardiovascular complications of immune checkpoint inhibitors for cancer. *Eur. Heart J.* **43**, 4458–4468 (2022).
- Laenens, D. et al. Incidence of Cardiovascular Events in Patients Treated With Immune Checkpoint Inhibitors. *J. Clin. Oncol.* **40**, 3430–3438 (2022).
- D'Souza, M. et al. The risk of cardiac events in patients receiving immune checkpoint inhibitors: a nationwide Danish study. *Eur. Heart J.* **42**, 1621–1631 (2021).
- Mahmood, S. S. et al. Myocarditis in Patients Treated With Immune Checkpoint Inhibitors. *J. Am. Coll. Cardiol.* **71**, 1755–1764 (2018).
- Axelrod, M. L. et al. T cells specific for alpha-myosin drive immunotherapy-related myocarditis. *Nature* **611**, 818–826 (2022).
- Wei, S. C. et al. A Genetic Mouse Model Recapitulates Immune Checkpoint Inhibitor-Associated Myocarditis and Supports a Mechanism-Based Therapeutic Intervention. *Cancer Discov.* **11**, 614–625 (2021).
- Won, T. et al. Cardiac myosin-specific autoimmune T cells contribute to immune-checkpoint-inhibitor-associated myocarditis. *Cell Rep.* **41**, 111611 (2022).
- Zhu, H. et al. Identification of Pathogenic Immune Cell Subsets Associated With Checkpoint Inhibitor-Induced Myocarditis. *Circulation* **146**, 316–335 (2022).
- Fenioux, C. et al. Thymus alterations and susceptibility to immune checkpoint inhibitor myocarditis. *Nat Med.* **29**, 3100–3110 (2023).
- Galluzzi, L. et al. Molecular mechanisms of cell death: recommendations of the Nomenclature Committee on Cell Death 2018. *Cell Death Differ.* **25**, 486–541 (2018).
- Man, S. M., Karki, R. & Kanneganti, T. D. Molecular mechanisms and functions of pyroptosis, inflammatory caspases and inflammasomes in infectious diseases. *Immunol. Rev.* **277**, 61–75 (2017).
- Shi, J. et al. Cleavage of GSDMD by inflammatory caspases determines pyroptotic cell death. *Nature* **526**, 660–665 (2015).
- Kayagaki, N. et al. Caspase-11 cleaves gasdermin D for non-canonical inflammasome signalling. *Nature* **526**, 666–671 (2015).
- Wang, Y. et al. Chemotherapy drugs induce pyroptosis through caspase-3 cleavage of a gasdermin. *Nature* **547**, 99–103 (2017).
- Zhang, Z. et al. Gasdermin E suppresses tumour growth by activating anti-tumour immunity. *Nature* **579**, 415–420 (2020).
- Liu, Y. et al. Gasdermin E-mediated target cell pyroptosis by CAR T cells triggers cytokine release syndrome. *Sci. Immunol.* **5**, eaax7969 (2020).
- Canna, S. W. et al. An activating NLR4 inflammasome mutation causes autoinflammation with recurrent macrophage activation syndrome. *Nat. Genet.* **46**, 1140–1146 (2014).
- Kanneganti, A. et al. GSDMD is critical for autoinflammatory pathology in a mouse model of Familial Mediterranean Fever. *J. Exp. Med.* **215**, 1519–1529 (2018).
- Rubio-Infante, N. et al. Cardiotoxicity associated with immune checkpoint inhibitor therapy: a meta-analysis. *Eur. J. Heart Fail.* **23**, 1739–1747 (2021).
- Lehmann, L. H. et al. Cardiomuscular Biomarkers in the Diagnosis and Prognostication of Immune Checkpoint Inhibitor Myocarditis. *Circulation* **148**, 473–486 (2023).
- Rogers, C. et al. Gasdermin pores permeabilize mitochondria to augment caspase-3 activation during apoptosis and inflammasome activation. *Nat. Commun.* **10**, 1689 (2019).
- Herrmann, J. et al. Defining cardiovascular toxicities of cancer therapies: an International Cardio-Oncology Society (IC-OS) consensus statement. *Eur. Heart J.* **43**, 280–299 (2022).
- Jiao, X. D. et al. Targeted therapy for intractable cancer on the basis of molecular profiles: An open-label, phase II basket trial (Long March Pathway). *Front Oncol.* **13**, 860711 (2023).
- Qin, B. D. et al. Pan-cancer efficacy and safety of anlotinib plus PD-1 inhibitor in refractory solid tumor: A single-arm, open-label, phase II trial. *Int J. Cancer* **153**, 815–825 (2023).
- Nishimura, H. et al. Autoimmune dilated cardiomyopathy in PD-1 receptor-deficient mice. *Science* **291**, 319–322 (2001).
- Okazaki, T. et al. Autoantibodies against cardiac troponin I are responsible for dilated cardiomyopathy in PD-1-deficient mice. *Nat. Med.* **9**, 1477–1483 (2003).
- Lozano, A. X. et al. T cell characteristics associated with toxicity to immune checkpoint blockade in patients with melanoma. *Nat. Med.* **28**, 353–362 (2022).
- Michel, L. et al. Targeting early stages of cardiotoxicity from anti-PD1 immune checkpoint inhibitor therapy. *Eur. Heart J.* **43**, 316–329 (2022).
- Ma, P. et al. Expansion of Pathogenic Cardiac Macrophages in Immune Checkpoint Inhibitor Myocarditis. *Circulation* **149**, 48–66 (2024).
- Weckbach, L. T. et al. Midkine drives cardiac inflammation by promoting neutrophil trafficking and NETosis in myocarditis. *J. Exp. Med.* **216**, 350–368 (2019).
- Wang, D. Y. et al. Fatal Toxic Effects Associated With Immune Checkpoint Inhibitors: A Systematic Review and Meta-analysis. *JAMA Oncol.* **4**, 1721–1728 (2018).
- Naqash, A. R. et al. Major Adverse Cardiac Events With Immune Checkpoint Inhibitors: A Pooled Analysis of Trials Sponsored by the National Cancer Institute-Cancer Therapy Evaluation Program. *J. Clin. Oncol.* **40**, 3439–3452 (2022).
- Zhang, Y. et al. Hormonal therapies up-regulate MANF and overcome female susceptibility to immune checkpoint inhibitor myocarditis. *Sci. Transl. Med.* **14**, eabo1981 (2022).
- Liu, M. et al. Soluble CTLA-4 mutants ameliorate immune-related adverse events but preserve efficacy of CTLA-4- and PD-1-targeted immunotherapy. *Sci. Transl. Med.* **15**, eabm5663 (2023).
- Dragatsis, I. & Zeitlin, S. A method for the generation of conditional gene repair mutations in mice. *Nucleic Acids Res.* **29**, E10 (2001).
- West, A. P. et al. Mitochondrial DNA stress primes the antiviral innate immune response. *Nature* **520**, 553–557 (2015).

39. Humphries, F. et al. Succination inactivates gasdermin D and blocks pyroptosis. *Science* **369**, 1633–1637 (2020).
40. Wong, A. & Epelman, S. Unchecked autoreactive CD8+ T cells wreak havoc in cancer immunotherapy. *Nat. Cardiovascular Res.* **1**, 1111–1113 (2022).
41. Nishimura, H., Nose, M., Hiai, H., Minato, N. & Honjo, T. Development of lupus-like autoimmune diseases by disruption of the PD-1 gene encoding an ITIM motif-carrying immunoreceptor. *Immunity* **11**, 141–151 (1999).
42. Xia, W. et al. PD-1 inhibitor inducing exosomal miR-34a-5p expression mediates the cross talk between cardiomyocyte and macrophage in immune checkpoint inhibitor-related cardiac dysfunction. *J. Immunother. Cancer* **8**, e001293 (2020).
43. Tsuruoka, K. et al. Exacerbation of autoimmune myocarditis by an immune checkpoint inhibitor is dependent on its time of administration in mice. *Int J. Cardiol.* **313**, 67–75 (2020).
44. Zhang, H. et al. Protective Effect of Crocin on Immune Checkpoint Inhibitors-Related Myocarditis Through Inhibiting NLRP3 Mediated Pyroptosis in Cardiomyocytes via NF-kappaB Pathway. *J. Inflamm. Res.* **15**, 1653–1666 (2022).
45. Salem, J. E. et al. Abatacept/Ruxolitinib and Screening for Concomitant Respiratory Muscle Failure to Mitigate Fatality of Immune-Checkpoint Inhibitor Myocarditis. *Cancer Discov.* **13**, 1100–1115 (2023).
46. Shah, D., Soper, B. & Shopland, L. Cytokine release syndrome and cancer immunotherapies - historical challenges and promising futures. *Front Immunol.* **14**, 1190379 (2023).
47. Deng, W. et al. Streptococcal pyrogenic exotoxin B cleaves GSDMA and triggers pyroptosis. *Nature* **602**, 496–502 (2022).
48. Rana, N. et al. GSDMB is increased in IBD and regulates epithelial restitution/repair independent of pyroptosis. *Cell* **185**, 283–298.e217 (2022).
49. Rogers, C. et al. Cleavage of DFNA5 by caspase-3 during apoptosis mediates progression to secondary necrotic/pyroptotic cell death. *Nat. Commun.* **8**, 14128 (2017).
50. Wei, Y. et al. GSDME-mediated pyroptosis promotes the progression and associated inflammation of atherosclerosis. *Nat. Commun.* **14**, 929 (2023).
51. Lin, J. et al. Oncolytic Parapoxvirus induces Gasdermin E-mediated pyroptosis and activates antitumor immunity. *Nat. Commun.* **14**, 224 (2023).
52. Shi, H. et al. GSDMD-Mediated Cardiomyocyte Pyroptosis Promotes Myocardial I/R Injury. *Circ. Res.* **129**, 383–396 (2021).
53. Jiang, K. et al. Gasdermin D inhibition confers antineutrophil-mediated cardioprotection in acute myocardial infarction. *J. Clin. Invest* **132**, e151268 (2022).
54. Van Laer, L. et al. Nonsyndromic hearing impairment is associated with a mutation in DFNA5. *Nat. Genet* **20**, 194–197 (1998).
55. Booth, K. T., Azaiez, H. & Smith, R. J. H. DFNA5 (GSDME) c.991-15\_991-13delTTC: Founder Mutation or Mutational Hotspot? *Int J. Mol. Sci.* **21**, 3951 (2020).
56. Nishio, A. et al. A DFNA5 mutation identified in Japanese families with autosomal dominant hereditary hearing loss. *Ann. Hum. Genet* **78**, 83–91 (2014).
57. Cheng, J. et al. A novel DFNA5 mutation, IVS8+4 A>G, in the splice donor site of intron 8 causes late-onset non-syndromic hearing loss in a Chinese family. *Clin. Genet* **72**, 471–477 (2007).
58. Van Laer, L. et al. A novel DFNA5 mutation does not cause hearing loss in an Iranian family. *J. Hum. Genet* **52**, 549–552 (2007).
59. Del Re, D. P., Amgalan, D., Linkermann, A., Liu, Q. & Kitsis, R. N. Fundamental Mechanisms of Regulated Cell Death and Implications for Heart Disease. *Physiol. Rev.* **99**, 1765–1817 (2019).
60. Chen, K. W. et al. RIPK1 activates distinct gasdermins in macrophages and neutrophils upon pathogen blockade of innate immune signaling. *Proc. Natl Acad. Sci. USA* **118**, e2101189118 (2021).
61. Sun, L., Wu, J., Du, F., Chen, X. & Chen, Z. J. Cyclic GMP-AMP synthase is a cytosolic DNA sensor that activates the type I interferon pathway. *Science* **339**, 786–791 (2013).
62. Cao, Q. et al. Pyroptosis, Metabolism, and Oxidation in Tumorigenesis: Mechanisms and Therapeutic Implications. *Antioxid. Redox Signal* **39**, 512–530 (2023).
63. Garland, K. M., Sheehy, T. L. & Wilson, J. T. Chemical and Biomolecular Strategies for STING Pathway Activation in Cancer Immunotherapy. *Chem. Rev.* **122**, 5977–6039 (2022).
64. Ramanjulu, J. M. et al. Design of amidobenzimidazole STING receptor agonists with systemic activity. *Nature* **564**, 439–443 (2018).
65. Pan, B. S. et al. An orally available non-nucleotide STING agonist with antitumor activity. *Science* **369**, eaba6098 (2020).
66. Lu, D. et al. Activation of STING by targeting a pocket in the transmembrane domain. *Nature* **604**, 557–562 (2022).
67. Kim, M. S. et al. Aberrant promoter methylation and tumor suppressive activity of the DFNA5 gene in colorectal carcinoma. *Oncogene* **27**, 3624–3634 (2008).
68. Gerdt, E. & Regitz-Zagrosek, V. Sex differences in cardiometabolic disorders. *Nat. Med.* **25**, 1657–1666 (2019).
69. Schiattarella, G. G. et al. Nitrosative stress drives heart failure with preserved ejection fraction. *Nature* **568**, 351–356 (2019).
70. Jia, D. et al. Interleukin-35 Promotes Macrophage Survival and Improves Wound Healing After Myocardial Infarction in Mice. *Circ. Res.* **124**, 1323–1336 (2019).
71. Ismahil, M. A. et al. Remodeling of the mononuclear phagocyte network underlies chronic inflammation and disease progression in heart failure: critical importance of the cardiosplenic axis. *Circ. Res.* **114**, 266–282 (2014).
72. Toghi Eshghi, S. et al. Quantitative Comparison of Conventional and t-SNE-guided Gating Analyses. *Front Immunol.* **10**, 1194 (2019).
73. Tong, J. et al. Targeting a novel inducible GPX4 alternative isoform to alleviate ferroptosis and treat metabolic-associated fatty liver disease. *Acta Pharm. Sin. B* **12**, 3650–3666 (2022).
74. Ji, Q. X. et al. Ferroptotic stress facilitates smooth muscle cell dedifferentiation in arterial remodelling by disrupting mitochondrial homeostasis. *Cell Death Differ.* **30**, 457–474 (2023).
75. Chi, C. et al. Exerkine fibronectin type-III domain-containing protein 5/irisin-enriched extracellular vesicles delay vascular ageing by increasing SIRT6 stability. *Eur. Heart J.* **43**, 4579–4595 (2022).

## Acknowledgements

Funding This work was supported by the grants from National Natural Science Foundation (82274030, 82273922, 82373927 and 82073915), National Key Research and Development Program Stem Cell and Translational Research Key Projects (2018YFA0108301), Shanghai Talent Development Fund (2020091), Shanghai Science and Technology Commission Grants (21XD1424900, 2020-JMRH1-KJ12, 19140904700 and 19140904900), Shanghai Shuguang Program (19SG32) and Shanghai Municipal Three Year Action Plan for Strengthening the Construction of Public Health System (GWV1-11.2-XD06).

## Author contributions

Conceptualization, P.W., F.M.S. and D.J.L.; resources, X.D.J. and Z.G.C.; methodology, S.J.S. and Q.C.; investigation, S.J.S., Q.C., J.H.Z., Q.R.S., Y.L., Z.Z., F.F.X., Y.S., J.T., S.X.O., J.T.F. and Y.Z.; writing, J.R., D.J.L., F.M.S. and P.W. All authors interpreted the data, revised the paper critically for important intellectual content and approved the final version of the manuscript.

## Competing interests

The authors declare no competing interests.



## Additional information

**Supplementary information** The online version contains supplementary material available at <https://doi.org/10.1038/s41467-024-50996-5>.

**Correspondence** and requests for materials should be addressed to Dong-Jie Li, Fu-Ming Shen or Pei Wang.

**Peer review information** *Nature Communications* thanks the anonymous reviewers for their contribution to the peer review of this work. A peer review file is available.

**Reprints and permissions information** is available at <http://www.nature.com/reprints>

**Publisher's note** Springer Nature remains neutral with regard to jurisdictional claims in published maps and institutional affiliations.

**Open Access** This article is licensed under a Creative Commons Attribution-NonCommercial-NoDerivatives 4.0 International License, which permits any non-commercial use, sharing, distribution and reproduction in any medium or format, as long as you give appropriate credit to the original author(s) and the source, provide a link to the Creative Commons licence, and indicate if you modified the licensed material. You do not have permission under this licence to share adapted material derived from this article or parts of it. The images or other third party material in this article are included in the article's Creative Commons licence, unless indicated otherwise in a credit line to the material. If material is not included in the article's Creative Commons licence and your intended use is not permitted by statutory regulation or exceeds the permitted use, you will need to obtain permission directly from the copyright holder. To view a copy of this licence, visit <http://creativecommons.org/licenses/by-nc-nd/4.0/>.

© The Author(s) 2024